INVESTIGATION OF FLUID STRUCTURE INTERACTION IN CARDIOVASCULAR SYSTEM FROM DIAGNOSTIC AND PATHOLOGICAL PERSPECTIVE

A THESIS SUBMITTED TO
THE GRADUATE SCHOOL OF NATURAL AND APPLIED SCIENCES
OF
MIDDLE EAST TECHNICAL UNIVERSITY

BY

HÜSEYİN ENES SALMAN

IN PARTIAL FULFILLMENT OF THE REQUIREMENTS
FOR
THE DEGREE OF MASTER OF SCIENCE
IN
MECHANICAL ENGINEERING

JUNE 2012

Approval of the thesis:

INVESTIGATION OF FLUID STRUCTURE INTERACTION IN CARDIOVASCULAR SYSTEM FROM DIAGNOSTIC AND PATHOLOGICAL PERSPECTIVE

submitted by **HÜSEYİN ENES SALMAN** in partial fulfillment of the requirements for the degree of **Master of Science in Mechanical Engineering, Middle East Technical University** by,

Prof. Dr. Canan Özgen
Dean, Graduate School of **Natural and Applied Sciences** __________________

Prof. Dr. Suha Oral
Head of the Department, **Mechanical Engineering** __________________

Assist. Prof. Dr. Yiğit Yazıcıoğlu
Supervisor, **Mechanical Engineering Dept., METU** __________________

Assist. Prof. Dr. Cüneyt Sert
Co-Supervisor, **Mechanical Engineering Dept., METU** __________________

Examining Committee Members:

Assist. Prof. Dr. Ender Ciğeroğlu
Mechanical Engineering Dept., METU __________________

Assist. Prof. Dr. Yiğit Yazıcıoğlu
Mechanical Engineering Dept., METU __________________

Assist. Prof. Dr. Cüneyt Sert
Mechanical Engineering Dept., METU __________________

Assist. Prof. Dr. Mehmet Metin Yavuz
Mechanical Engineering Dept., METU __________________

Assist. Prof. Dr. Mehmet Bülent Özer
Mechanical Engineering Dept., TOBB ETU __________________

Date: 14.06.2012

I hereby declare that all information in this document has been obtained and presented in accordance with academic rules and ethical conduct. I also declare that, as required by these rules and conduct, I have fully cited and referenced all material and results that are not original to this work.

Name, Last name: Hüseyin Enes, Salman

Signature:

ABSTRACT

INVESTIGATION OF FLUID STRUCTURE INTERACTION IN CARDIOVASCULAR SYSTEM FROM DIAGNOSTIC AND PATHOLOGICAL PERSPECTIVE

Salman, Hüseyin Enes

M.Sc., Department of Mechanical Engineering
Supervisor: Assist. Prof. Dr. Yiğit Yazıcıoğlu
Co-Supervisor: Assist. Prof. Dr. Cüneyt Sert

June 2012, 108 pages

Atherosclerosis is a disease of the cardiovascular system where a stenosis may develop in an artery which is an abnormal narrowing in the blood vessel that adversely affects the blood flow. Due to the constriction of the blood vessel, the flow is disturbed, forming a jet and recirculation downstream of the stenosis. Dynamic pressure fluctuations on the inner wall of the blood vessel leads to the vibration of the vessel structure and acoustic energy is propagated through the surrounding tissue that can be detected on the skin surface. Acoustic energy radiating from the interaction of blood flow and stenotic blood vessel carries valuable information from a diagnostic perspective. In this study, a constricted blood flow is modeled by using ADINA finite element analysis software together with the blood vessel in the form of a thin cylindrical shell with an idealized blunt constriction. The flow is considered as incompressible and Newtonian. Water properties at indoor temperature are used for the fluid model. The diameter of the modeled vessel is 6.4 mm with 87% area reduction at the throat of the stenosis. The flow is investigated for Reynolds numbers

1000 and 2000. The problem is handled in three parts which are rigid wall Computational Fluid Dynamics (CFD) solution, structural analysis of fluid filled cylindrical shell, and Fluid Structure Interaction (FSI) solutions of fluid flow and vessel structure. The pressure fluctuations and consequential vessel wall vibrations display broadband spectral content over a range of several hundred Hz with strong fluid-structural coupling. Maximum dynamic pressure and vibration amplitudes are observed around the reattachment point of the flow near the exit of the stenosis and this effect gradually decreases along downstream of flow. Results obtained by the numerical simulations are compared with relevant studies in the literature and it is concluded that ADINA can be used to investigate these types of problems involving high frequency pressure fluctuations of the fluid and the resulting vibratory motion of the surrounding blood vessel structure.

Keywords: Fluid Structure Interaction, Blood Flow Simulation, Stenosis, Vessel Wall Vibration

ÖZ

DOLAŞIM SİSTEMİNDEKİ KAN AKIŞI İLE DAMARLAR ARASINDAKİ ETKİLEŞİMLERİN PATOLOJİK VE TANISAL YÖNLERDEN İNCELENMESİ

Salman, Hüseyin Enes
Yüksek Lisans, Makina Mühendisliği Bölümü
Tez Yöneticisi: Yrd. Doç. Dr. Yiğit Yazıcıoğlu
Ortak Tez Yöneticisi: Yrd. Doç. Dr. Cüneyt Sert

Haziran 2012, 108 sayfa

Ateroskleroz, atardamarda oluşan anormal bir daralma sebebiyle kan akışını olumsuz etkileyen bir dolaşım sistemi hastalığıdır. Kan damarındaki daralma nedeniyle, akış düzensizleşerek akış yönünde bir püskürme ve devridaim bölgesi oluşur. Kan damarının iç duvarı üzerinde dinamik basınç dalgalanmaları damar yapısının titreşmesine yol açar ve oluşan akustik enerji damarı çevreleyen doku yoluyla deriye kadar yayılır ve deride tesbit edilebilir. Kan akışı ve tıkanık damar etkileşimi ile yayılan akustik enerji tanı koymak açısından değerli bilgiler taşır. Bu çalışmada kan akışı ince silindirik bir tıkanık damar yapısı ile birlikte ADİNA sonlu elemanlar programı kullanılarak modellenmiştir. Akış modeli için sıkıştırılamaz ve Newton kanununa uyumlu bir akışkan düşünülmüştür. Akışkan modeli için oda sıcaklığındaki suyun fiziksel özellikleri kullanılmıştır. Modellenen damar yapısının çapı 6.4 mm olarak oluşturulmuş ve tıkanıklık bölgesinde akış alanı %87 daraltılmıştır. Akış simülasyonları Reynolds sayıları 1000 ve 2000 için incelenmiştir. Problem 3 bölümde ele alınmıştır. Bunlar rijit damar duvarı ile hesaplamalı akışkanlar dinamiği çözümü, sıvı dolu silindirik yapıdaki damarın yapısal analizi ve sıvı akışı ve esnek damar yapısının katı-sıvı etkileşimi ile çözümleridir. Basınç dalgalanmaları ve damar duvarı titreşimlerinin birkaç yüz Hz aralığındaki katı-sıvı etkileşimi içeriği görüntülenmiştir. Maksimum dinamik basınç ve titreşim genlikleri darlık çıkışının yakınında gözlenmiştir ve genliklerin akış yönü boyunca giderek düştüğü görülmüştür. Elde edilen sayısal sonuçlar, literatürdeki ilgili çalışmaların sonuçları ile karşılaştırılmıştır ve ADİNA programının yüksek frekanslı basınç dalgalanmaları ve titreşim hareketleri içeren bu tür problemlerde modelleme için kullanılabileceği sonucuna varılmıştır.

Anahtar Kelimeler: Katı Sıvı Etkileşimi, Kan Akış Simülasyonu, Damar Daralması, Damar Duvarı Titreşimi

To My Family

ACKNOWLEDGEMENTS

First of all, I would like to express my deepest gratitude to my supervisor Assist. Prof. Dr. Yiğit Yazıcıoğlu and my co-supervisor Assist. Prof. Dr. Cüneyt Sert for their guidance, criticism, encouragements, advice and insight throughout my research.

I also would like to thank my colleague and roommate Tolga Özaslan for his moral support and encouragement. Special thanks go to my colleagues Kamil Özden and Mashar Tekin for their support and encouragement.

Finally, I am deeply grateful to my family for their faith in me. Especially I would like to thank my father who is an experienced cardiovascular surgeon, for sharing his experiences and valuable comments with me and encouraged me to study on this research.

TABLE OF CONTENTS

LIST OF TABLES

TABLES

LIST OF FIGURES

FIGURES

CHAPTER 1

INTRODUCTION

1.1. Problem Definition

Atherosclerosis is a chronic inflammatory disease affecting blood vessels where arterial wall thickens due to the accumulation of fatty materials such as cholesterol [1]. Atherosclerotic lesions chronically expand asymptomatically and a soft plaque may rupture forming a thrombus (form of blood between fluid and solid). Intraluminal thrombi can move into the circulation, occluding smaller vessels causing sudden thromboembolism. Apart from thromboembolism, atherosclerotic lesions can grow until blood flow is severely reduced or cause complete closure of the lumen resulting in ischemia (inadequate blood supply). In the event of an infarction by any of the mechanisms mentioned above, the tissues fed by the artery will die in the matter of several minutes. Atherosclerosis can occur anywhere in the circulatory system such as arteries feeding the brain, heart, kidneys, legs, etc. The decreased blood supply may be "clinically silent" and affect a small and unimportant part of the body or jeopardize a vital organ or system. Atherosclerosis is usually found in most major arteries and it typically begins in early adolescence. For the most part of the population, it is left undetected by most diagnostic methods during early years of life. Depending on the location of atherosclerotic lesions, Coronary Artery Disease (CAD), Stroke or Peripheral Artery Occlusive Disease (PAOD) may develop. Coronary Artery Disease (CAD) results from plaque accumulation on the inner walls of the coronary arteries that feed the myocardium (heart muscle). The symptoms of this disease are usually manifested in the advanced stage but most individuals with CAD show no evidence for decades. After years of silent progression, plaques may rupture and restrict blood flow to the heart muscle. CAD is not only the leading cause of death worldwide, but it is also the most common cause of sudden death, and is also the most common reason for death of men and women over 20 years of age [2].

Stroke or Cerebrovascular Accident (CVA) is the rapid loss of brain functions due to decrease in the blood supply to the brain due to ischemia caused by a blockage or a hemorrhage. Affected area of the brain will be unable to function, resulting in impaired motor, sensory, communication and cognitive abilities. A stroke can cause permanent disabilities and death. It is the leading cause of adult disability in the United States and Europe and the second leading cause of death worldwide [3].

PAOD is the obstruction of arteries other than the ones related to the heart and the brain. It usually refers to the condition of insufficient blood supply to the legs, arms and other vital organs. Individuals with PAOD have a low risk to develop severe ischemia and require amputation but carry a higher risk for other potentially more serious cardiovascular events such as CAD and Stroke. Large-vessel PAOD increases mortality from cardiovascular disease significantly. Patients with PAOD carries a greater than 20% risk of a coronary event in 10 years [4].

Cardiovascular disease is usually detected by cardiac stress testing and/or angiography. Interestingly, cardiac stress testing can detect only lumen narrowing of ~75% or greater. In addition, angioplasty is performed when there is a suspicion of severe arterial blockage because of the invasive nature of this procedure. Therefore, these methods focus on detecting only severe stenosis whereas most flow disruption start occurring before 50% lumen narrowing takes place with an average of about 20% stenosis [5, 6].

It has to be also noted that, there may be arterial locations with heavy plaque formation that do not result in lumen narrowing. Here the plaque can still rupture and cause a sudden occlusion in the lumen.

Treatments for atherosclerosis are the relatively less invasive angioplasty procedures and majorly invasive bypass surgery. These treatments are usually administered at the later stages of the disease due to the capabilities of the current diagnostic techniques. It would be preferred to detect the disease much earlier and take preventative actions by making lifestyle changes before significant amount of vascular damage takes place. Considering the aforementioned disorders, it becomes critical to diagnose the stenotic narrowing at an early stage.

The common method for diagnosing a stenosis is arteriography [7]. The basis of arteriography is the injection of an X-ray contrast agent into the body and obtaining the X-ray image, by which the place of stenosis and degree of narrowing can be detected. In Figure 1.1, a view of diseased artery detected by the method of arteriography is provided.

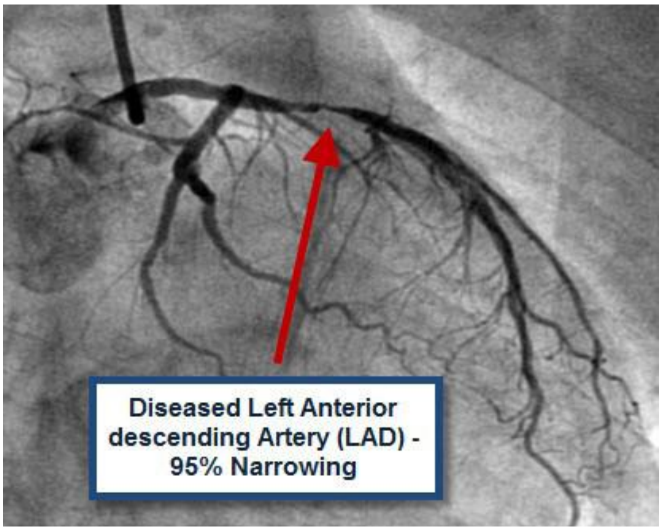

Figure 1.1 The method of arteriography

Although arteriography is the most common method for diagnosing a stenosis, there are some disadvantages of this method. First of all, it is an invasive method in which a catheter has to be placed close to the suspected location of the stenosis, which may lead to bleeding or infection after the operation. Also, arteriography is applied when stenosis shows clinical symptoms [7, 8]. Before the clinical symptoms, this method is not preferred, which means it is not a preventive method. It is used to understand the degree of the disease, not to prevent the disease. In addition, X-ray angiography becomes error-prone if the blood vessel geometry is noncircular since it employs a projected view of vessel geometry [9, 10].

As an alternative non-invasive diagnosing method, "phonoangiography" is proposed by Lees and Dewey [11]. The method of phonoangiography makes use of the acoustic radiation due to the abnormal flow conditions in the blood flow and it is studied and applied extensively [12, 13, 14, 15]. Nearly all of the authors stated that the reason of abnormal flow conditions in a stenosed flow is disturbed flow characteristics and the main source of the vascular noise field is found to be the turbulent pressure fluctuations in the blood vessel [8, 12, 13, 14, 16, 17]. The basic idea of phonoangiography is represented in Figure 1.2.

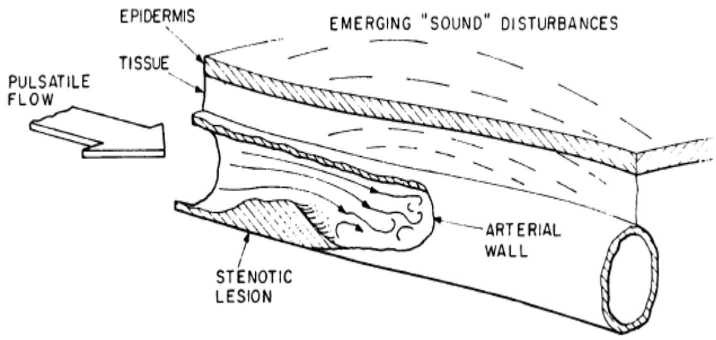

Figure 1.2 Acoustic radiation from a stenotic artery [11]

When passing over a stenotic lesion, the regular flow character of fluid changes due to the constriction. The flow velocity increases and a fluid jet is formed at the throat of stenosis. A chaotic behavior prevails downstream of the flow for a certain range. Since the vessel structure interacts with the fluid, it vibrates due to the flow conditions and a vascular sound is present. The vascular sounds emitted from the blood vessels are called "murmurs". The noise field induced inside the blood vessel, filtered by the vessel structure propagates through tissue, and finally reaches the skin [8, 14]. By measuring the sound waves on the skin surface, it is possible to gather information related with the flow inside the vessel and this information can be used for diagnostic purposes. The method of phonoangiography is a non-invasive diagnostic technique which can be used to obtain information about fundamental mechanisms of vascular sound generation and sound transmission to the skin surface.

1.2. The Objective

The main goal of this work is to investigate the flow in a stenosed vessel to obtain pressure fluctuations at the vessel wall and vibration of the vessel structure by using a numerical model. The problem is handled as a Fluid-Structure Interaction (FSI) problem and solved using computational techniques. Flow analysis is performed by using a commercial software which is capable of carrying out FSI analysis. The pressure fluctuations on the vessel wall and the resulting transverse vessel wall vibratory displacements are sought. Spectral characteristics of the pressure fluctuations and blood vessel wall vibrations are obtained and compared with the results in literature [7].

The characteristic signatures and sharp changes in the acoustic field may provide beneficial insight for diagnosing the stenosis. The results are expected to contribute to the understanding of the conditions of a stenosed flow which can be used in diagnosing the stenosis in a blood vessel by the method of phonoangiography.

The flow in rigid and flexible blood vessels are analyzed separately for comparison purposes. The effect of atherosclerosis, which is the obstruction in the blood vessel is investigated for both cases. Modal analysis is performed for simplified cylindrical shell type model of blood vessels. The investigation is focused on results which can be used for medical purposes. Information gathered from the numerical simulations may be used to further understand and explain the existing in vivo data, and by that way it may be possible to develop more accurate imaging and diagnostic techniques [9, 18].

1.3. Scope of the Thesis

In order to achieve the goal of this study, numerical simulations of a stenosed flow are performed using Automatic Dynamic Incremental Nonlinear Analysis (ADINA) (ADINA R&D Inc., Watertown, MA, USA) which is a finite element software capable of solving FSI problems. Numerical simulations are applied for a simple, stenosed blood vessel-like geometry, which is commonly used in experimental studies in literature. By this way, the results of numerical simulations can be compared with the experimental results.

First, rigid wall assumption is applied in numerical models for two different Reynolds numbers, 1000 and 2000, respectively. In numerical models water is used as fluid instead of blood since the properties of water at indoor temperature are similar to properties of blood. After the rigid wall assumption, the vessel is modeled as an elastic structure by using properties of latex rubber material. The vessel can deform due to the flow inside it. The elastic structure model and fluid model is then coupled and FSI analysis is conducted. As a result, it is possible to predict the vibrations on the vessel structure. Modal analysis of the vessel structure is carried out and the natural frequencies and mode shapes of the structure is compared with the FSI analysis results. In order to obtain the unsteady, turbulent flow field, LES (Large Eddy Simulation) and DES (Detached Eddy Simulation) models are used.

1.4. Overview

This study is composed of five chapters. In the first chapter, the problem is introduced and the methodology to be used is explained. The past studies in literature are summarized and a brief background information is given in the second chapter. Third chapter is about the fluid dynamics equations and turbulence models that will be used in the numerical simulations. Fourth chapter presents the obtained results and compares them with the findings of similar studies in literature in order to validate the numerical model. Finally, conclusions are drawn in the fifth chapter, summarizing the work and suggesting directions for future studies.

CHAPTER 2

BACKGROUND

Turbulence induced vessel wall vibrations are encountered where there is fluid flow through a deformable structure containing an obstruction. In oil and gas transportation, pipe vibrations related with fluid flow has been of great interest. These vibrations can lead to fractures and failure in piping systems. In the same manner, cardiovascular system is a similar fluid transportation system in which blood interacts with the vessels. The dynamic behavior of the vessels under fluidic excitation can be estimated by computational methods with FSI capabilities. In this chapter the physics behind FSI analysis will be explained and analytical, experimental, and numerical techniques used to model turbulence induced pressure fluctuations at the vessel wall are reviewed.

2.1. Fluid-Structure Interaction (FSI)

In the stenosed region of a blood vessel, decreased flow area results in an increased average velocity. Blood leaves the stenosed region as a high speed turbulent jet. Pressure fluctuations seen in the downstream of the stenosis are due to the turbulent flow characteristics [8, 12, 13, 14, 16, 17]. The vessel structure accordingly vibrates as a response to the turbulence induced pressure fluctuations.

In order to obtain the vibration and deformation on the vessel structure due to flow conditions, a fluid-structure coupled analysis should be performed. The procedure of a typical iterative FSI analysis is presented in Figure 2.1.

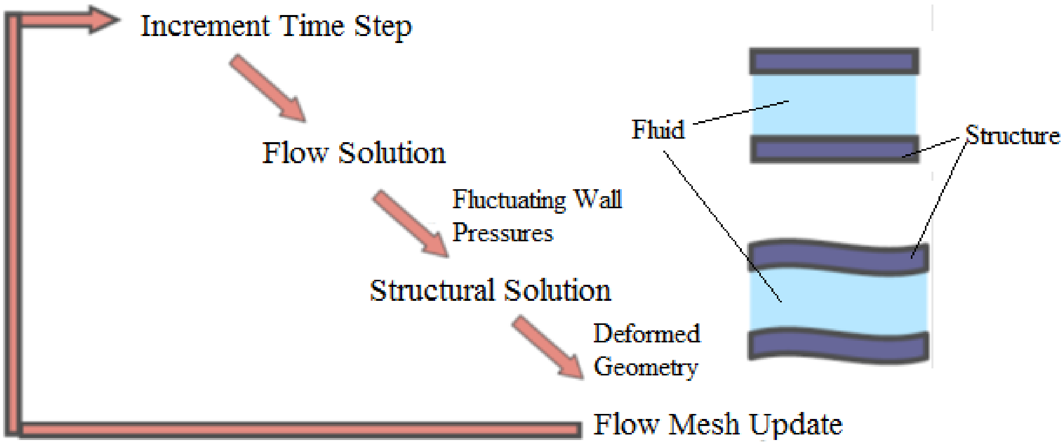

Figure 2.1 Solution procedure for an iterative FSI analysis [19]

For the iterative FSI analysis of flow in a deformable blood vessel, first the fluid flow variables are solved for an incremental time step and the pressure distribution on solid surfaces (walls) are obtained. As the next step, the forcing due to wall pressure is coupled with structure of the vessel and the geometry of the vessel is changed due to the applied pressure. Then the deformed shape of the structure, and therefore the flow domain, is determined and the flow and structure mesh is updated. These steps are than repeated for a new incremental time step.

There are several commercial software packages which are capable of solving FSI problems, e.g. ADINA, ALGOR, ANSYS, FIDAP, IFSAS, STRACO, SYSNOISE. In this thesis ADINA software is used.

2.2. Analytical Studies

In analytical studies, a closed form solution may be obtained, but simplifying assumptions have to be made for the complicated turbulent flow. The problem domain also has to be selected as a simple geometry which does not exactly represent the reality.

Borisyuk developed an acoustic model of human chest considering the presence of a stenotic obstruction and elastic properties of the vessel [16]. Acoustic generation and transmission of noise from the source to the receiver is considered and a simple stenotic narrowing of a vessel is assumed. The acoustic power spectrum for normal and stenosed vessel models are determined and characteristic signs of existence of the vessel constriction have been found. It has also been found that mild thickening of the vessel leads noticeable increase in the sound level and a shift of the peaks at the resonance frequencies in the acoustic spectrum. A 30% decrease in the diameter of the vessel, nearly 50% of area reduction, results in a 10-fold increase in the radiated acoustic power.

2.3. Experimental Studies

Experimental studies conducted in literature are mostly related with the flow downstream of the stenosis. In rigid tubes, it is observed that there are recirculation regions and turbulent downstream flow after the stenosed part [20].

Yazicioglu et al. studied the vibration of thin-walled viscoelastic tube theoretically and experimentally [21]. The vibration is due to a constriction in the tube which leads turbulent flow. Vibration of the tube is considered with coupling to internal flow and external tissue-like viscoelastic material or stagnant fluid. Analytical predictions and experimental results obtained by using LDV (Laser Doppler Vibrometry) are compared. It is stated discrepancies between theory and experiment is related with the linear structural model of the tube which do not capture the apparent non-linear phenomena that is highly dependent upon the mean pressure within the tube.

The schematic of the experimental setup for this study is given in Figure 2.2 [21]. In this setup, there are two reservoirs where the above reservoir is supply reservoir and by changing the height difference between two reservoirs, flow conditions in the vessel model can be adjusted for the desired flow rate and dynamic pressure. The compliant tube is placed on the flow path between the two reservoirs and the pressure and vibration inside and on the tube are measured by using a catheter type pressure transducer and LDV, respectively. The data obtained from the measurements are processed and the frequency spectrum of the pressure and vibration are obtained.

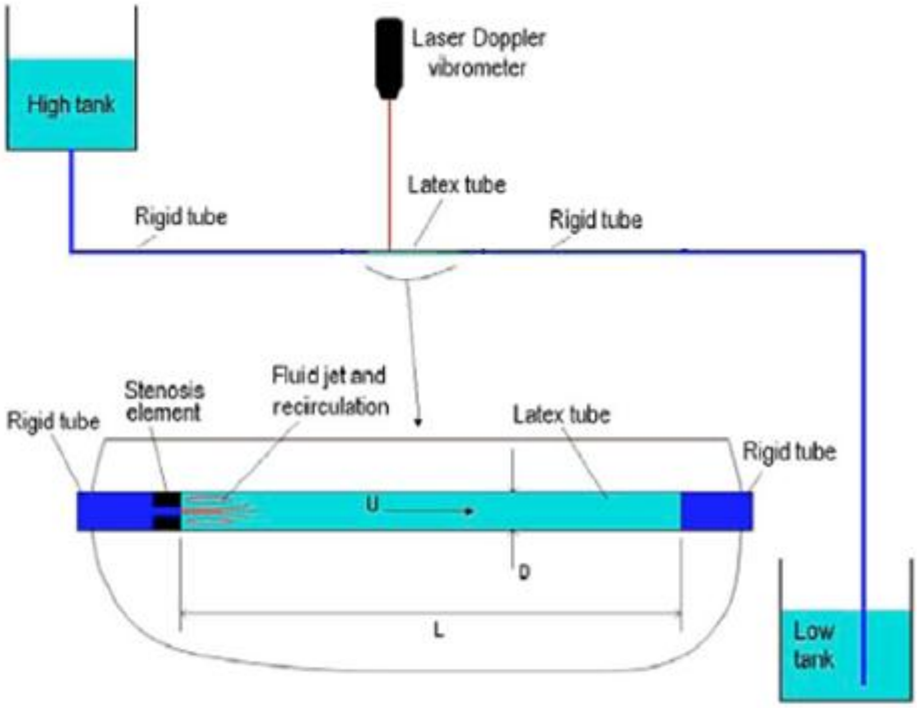

Figure 2.2 Scheme of experimental system [21]

Borisyuk carried out in-vitro experiments in order to investigate the properties of an acoustic field in the human chest [17]. In his study, unconstricted and partially occluded vessels are studied. Abrupt rigid-wall hollow axisymmetric cylindrical plugs with various inner diameters and lengths are used as the stenosis. It is found that there is a general increase of the noise level and production of new frequency components in power spectrum with increasing stenosis. This condition is a characteristic sign of the presence of an obstruction in vessel. Acoustic power generated by the stenosis is found as approximately proportional to the fourth power of the constriction severity and fourth power of the Reynolds number of the flow.

Tobin and Chang obtained wall pressure spectra at various positions downstream of axisymmetric cylindrical stenoses [22]. The focus of their investigation was developing a non-invasive clinical diagnostic technique capable of determining the degree of the stenosis from an analysis of the murmurs which are the sounds emitted from vessels associated with stenosis. They placed an obstruction inside a latex rubber tube which contains a steady water flow. Stenoses of different degrees of severity are used over a range of Reynolds numbers. For physiologically relevant Reynolds numbers, during peak systole a jet is observed from the stenosis throat which reattaches to the tube wall within 2.5 tube diameters from the stenosis. They found good universal correlations between spectrum frequency and pressure amplitude with degree of stenosis. A universal power spectral density function at the position of maximum wall pressure fluctuations is achieved by using new set of non-dimensional variables. They compared universal spectral density function with that of maximum Root Mean Square (RMS) wall pressure. These spectra are similar but not identical.

The results found in our numerical solutions will be compared with the results of Tobin and Chang [22] and Yazicioglu et al. [21]. Therefore the material properties and flow conditions are selected similar to those used in these experimental studies for the easiness of comparison.

2.4. Numerical Studies

Lee et al. [23] examined blood flow dynamics of a carotid bifurcation by a numerical simulation using the spectral element method. Pulsatile inlet conditions based on in vivo color Doppler ultrasound measurements of blood velocity are applied. It is stated that regions downstream of severe constriction can have significantly different biomechanical environment when compared with healthy blood vessels due to turbulence. At post stenotic region of internal carotid artery during systole when the blood is pumped to the body, transitional or weakly turbulent state of blood flow is obtained. During diastole, laminar flow is seen and during the deceleration of diastole, high frequency vortex shedding was greatest downstream of the stenosis. Velocity fluctuation frequencies were in the audible range of 100-300 Hz. This study investigates turbulence levels, complex flow field and biomechanical stresses present within a stenosed carotid artery.

Khanafer and Berguer [24] studied turbulent pulsatile flow and wall mechanics numerically by using an axisymmetric three-layered wall model of descending aorta. A fully coupled Fluid-Structure analysis is conducted in the investigation. The researchers obtained Von Mises wall stresses, streamlines and fluid pressure contours. According to the results, the peak wall stress and maximum shear stress is observed in the media part (the middle layer of the wall of a blood vessel) of the vessel. An arbitrary Lagrangian-Eulerian formulation is used for the analysis. A finite element formulation based on the Galerkin method was used to solve the governing equations of FSI model using ADINA software.

Tang et al. [25] studied and solved a three dimensional thick-wall model with FSI using ADINA software. Wall stress-strain distributions and flow parameters in carotid arteries with symmetric and asymmetric stenoses were obtained by numerical simulations. According to the results, stenosis caused considerable compressive stresses in the tube wall which may be related to the plaque cap rupture. Tube asymmetry and stenosis severity have important effects on flow and stress-strain distributions. Three-dimensional wall deformation, flow pressure, velocity and shear stress fields are investigated in the study.

Valencia and Villanueva [26] investigated flows in symmetric and asymmetric stenotic arteries. In this work, the unsteady non-Newtonian blood flow and mass transfer is in interest. Simulations are conducted by using ADINA, employing FSI. It is stated that FSI have significant influence on the hemodynamics of the stenotic arteries models. Stenosis geometry and severity changes the length of the recirculation region.

Tang et al. [27] performed numerical simulations in order to quantify the compressive conditions at constricted regions. If the severity of the stenosis is high, arteries may compress under physiologic conditions due to mean pressure drop. A nonlinear axisymmetric model is presented to simulate the flow in a compliant tube. ADINA is used to solve FSI model. The results indicate that severe stenosis lead to critical flow conditions as pressure drop, artery compression, plaque cap rupture and thrombus formation. A complex pressure field is found near stenosis which can not be resolved in one-dimensional models. For different pressure drop conditions, flow rates are calculated and compared with experimental results. For pre-buckling stage a reasonable agreement is found.

Shurtz [28] performed a LES model coupled with a finite element structural model in order to simulate FSI. Pipe vibration resulting from turbulent flow is analyzed. The results indicate that pipe wall acceleration is inversely dependent of pipe wall thickness. The dynamic effects influence long pipe and a respond through bending modes is present.

2.5. Research Contribution

One of the methods except RANS (Reynolds averaged Navier-Stokes equations) should be applied for resolving the fluctuating wall pressure. In this study, DES and LES models are used for the fluid flow. The basis for this decision is the affordable computational cost and obtaining accurate results with employing a coarser grid when compared with DNS (Direct numerical simulation).

As seen in Section 2.4, numerous of FSI problems are modeled and solved in literature. Transient analyses encountered in literature mostly use large time steps. In this investigation a time increment in the order of 10^{-4} seconds is used in order to capture the spectral distribution of the amplitudes of the frequency up to several hundred Hz. The FSI studies in literature are interested in the compression and enlargement of blood vessels due to events in the frequential scale of the cardiac cycle which is on the order of several Hz. In this thesis, the cardiac cycle is not considered and fluctuations due to turbulence is in interest which is different from most of the numerical simulations in the literature. In literature, many studies are related with stress and strain distributions on the vessel which is not within the scope of this study.

In this study, a stenosed flow model is developed using ADINA software. First, by using rigid wall assumption, wall pressure fluctuations in the flow are determined. In addition, FSI model is developed in order to obtain wall vibrations of the vessel structure. The numerical results are compared with the results in literature which have used the similar flow parameters and geometries.

CHAPTER 3

FLUID DYNAMICS, TURBULENCE MODELING, MODELED CASES & GEOMETRY

3.1. Description of Flow

Flow variables can be defined with magnitude and direction in space by using Lagrangian or Eulerian representations. In Lagrangian representation, individual fluid particles are observed through time and space. It can be explained by moving with fluid particle which is moving in a flow field and observing the properties of that particle as it changes its position and as time elapses. In Eulerian representation, the focus is on specific locations in the space of fluid flow instead of individual flow particles. Also, this system can be imagined as sitting on a fixed location and observing the fluid flow from that fixed place. When solving fluid dynamics problems, Eulerian representation is preferred since it is more practical than tracing a fluid particle towards downstream [29].

3.2. Governing Equations in Fluid Mechanics

3.2.1. Equations of Stress

Solids can sustain deviatoric stresses at rest. Deviatoric stress which is also known as differential stress, is a condition where the stress components at a point differ with direction. On the contrary, fluids can not sustain deviatoric stresses at rest. The only possible stress is hydrostatic pressure and is known as pressure [29]. In studying the motion of flow the most important independent variable is the velocity vector, $\boldsymbol{u}$, with three components shown below

$$u^T = [u_1, u_2, u_3]. \tag{3.1}$$

In solids, displacement variable has fundamental importance but in fluids velocity variable is more convenient to work with. The rate of strain, ε', is defined as,

$$\varepsilon'_{ij} = \frac{1}{2}\left(\frac{\partial u_i}{\partial x_j} + \frac{\partial u_j}{\partial x_i}\right). \tag{3.2}$$

If the fluid is incompressible and the viscosity is considered to be constant, then the tensor of shear stress can be defined as,

$$\tau_{ij} = \mu\left(\frac{\partial u_i}{\partial x_j} + \frac{\partial u_j}{\partial x_i}\right) \tag{3.3}$$

where μ is the viscosity of the fluid. The tensor of shear stress can be combined with the pressure field to obtain the following total stress tensor.

$$\sigma_{ij} = -p\delta_{ij} + \tau_{ij} \tag{3.4}$$

where τ_{ij} is the shear stress on i^{th} face (face which has unit normal vector in the i^{th} direction) and j^{th} direction of a fluid element, u_i is the velocity in the i^{th} direction, x_i is the i^{th} coordinate direction and p is the thermodynamic pressure. If this relation is not satisfied by the flow, then the flow is called 'non-Newtonian' in which the coefficient, μ, depends on strain rates. For a non-Newtonian fluid, the relation between shear stress and shear rate is not linear, therefore a constant viscosity can not be defined. Fluid viscosity in general depends on pressure and temperature for a Newtonian fluid, but not on forces acting upon the fluid.

Blood (cells and plasma) exhibits non-Newtonian fluid dynamics. But blood can be considered as Newtonian fluid at high shear rates above 50 s^{-1} which is commonly present in larger arteries [8]. The shear rate of a Newtonian fluid flowing within a pipe is defined as [30],

$$\dot{\gamma} = \frac{8u}{d} \tag{3.5}$$

where $\dot{\gamma}$ is the shear rate, u is the linear fluid velocity and d is the diameter of the pipe. In our flow models, the shear rates are approximately 195 s^{-1} and 390 s^{-1} for Reynolds numbers 1000 and 2000 respectively. The difference in viscosity between blood and water is compensated by choice of such flow velocities at which blood and water flows are similar [16]. Differences between non-Newtonian and Newtonian models are important at the regions having low velocity.

3.2.2. Conservation of Mass

Consider the control volume shown in Figure 3.1, which is fixed in space with its faces open to material transport. According to conservation of mass, time rate of change of the density in such a control volume is equal to the balance of incoming and leaving mass through the faces. For incompressible flows, the change in density over time vanishes and equation of conservation of mass can be described as,

$$\nabla \cdot \boldsymbol{u} = 0 \tag{3.6}$$

where ∇ is the gradient operator given by,

$$\nabla = \frac{\partial}{\partial x}\mathbf{i} + \frac{\partial}{\partial y}\mathbf{j} + \frac{\partial}{\partial z}\mathbf{k} \tag{3.7}$$

where **i**, **j**, **k** are the unit vectors.

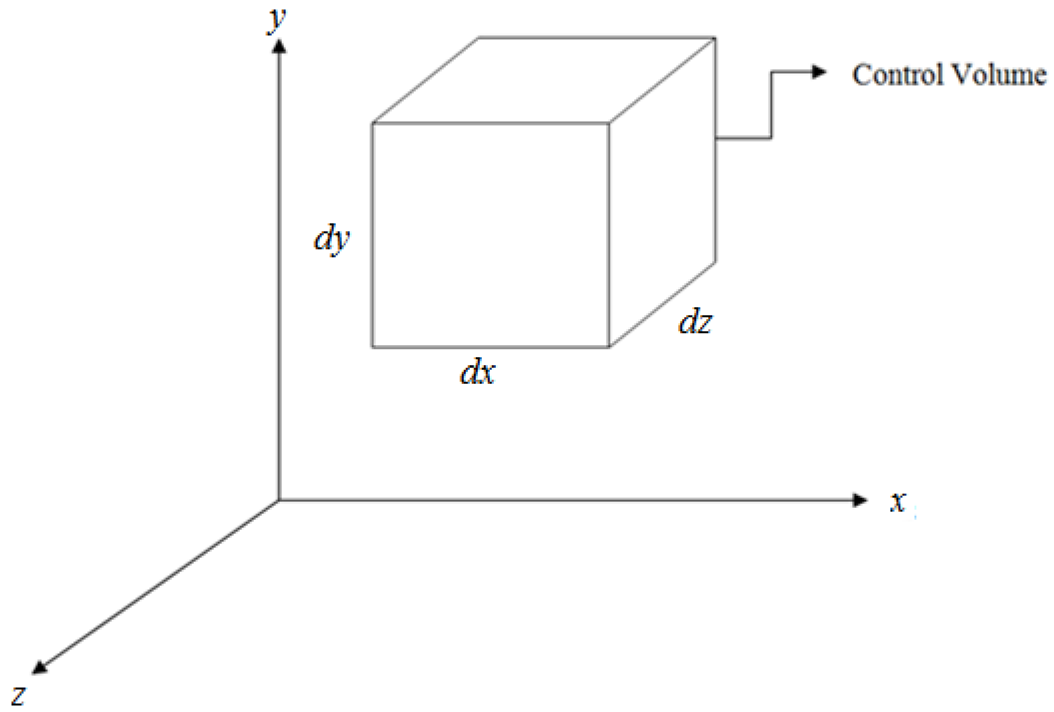

Figure 3.1 Control volume and coordinate system

3.2.3. Conservation of Momentum

In all directions, the stresses, σ_{ij}, and body forces, ρg_j, must be in equilibrium with balance of incoming and leaving linear equilibrium through the control volume. For each axis, the equations can be described as the following:

$$\rho\left(\frac{\partial u_x}{\partial t}+u_x\frac{\partial u_x}{\partial x}+u_y\frac{\partial u_x}{\partial y}+u_z\frac{\partial u_x}{\partial z}\right)=\mu\left(\frac{\partial^2 u_x}{\partial x^2}+\frac{\partial^2 u_x}{\partial y^2}+\frac{\partial^2 u_x}{\partial z^2}\right)-\frac{\partial p}{\partial x}+\rho g_x, \qquad (3.8)$$

$$\rho\left(\frac{\partial u_y}{\partial t}+u_x\frac{\partial u_y}{\partial x}+u_y\frac{\partial u_y}{\partial y}+u_z\frac{\partial u_y}{\partial z}\right)=\mu\left(\frac{\partial^2 u_y}{\partial x^2}+\frac{\partial^2 u_y}{\partial y^2}+\frac{\partial^2 u_y}{\partial z^2}\right)-\frac{\partial p}{\partial y}+\rho g_y, \qquad (3.9)$$

$$\rho\left(\frac{\partial u_z}{\partial t}+u_x\frac{\partial u_z}{\partial x}+u_y\frac{\partial u_z}{\partial y}+u_z\frac{\partial u_z}{\partial z}\right)=\mu\left(\frac{\partial^2 u_z}{\partial x^2}+\frac{\partial^2 u_z}{\partial y^2}+\frac{\partial^2 u_z}{\partial z^2}\right)-\frac{\partial p}{\partial z}+\rho g_z. \qquad (3.10)$$

3.3. Turbulence Models

Presence of a stenosis affects the flow characteristics, lead abnormal conditions and vascular noise field. The reason of these effects are found to be the turbulent pressure fluctuations in the stenotic flow [8, 12, 13, 14, 16, 17]. Therefore an appropriate turbulent model should be used in order to obtain turbulent induced blood vessel vibrations and instantaneous dynamic behavior of the flow. The turbulence can be viewed as an unsteady, three-dimensional, chaotic and non-linear phenomena. There is a chaotic behavior in turbulence but it is not random. Prediction of turbulence is a challenging problem in physics. The most challenging part of turbulence modeling is the prediction of growth and separation of boundary layer and prediction of momentum transfer after separation, which is very important for the stenosed vessel problem [31].

In some strategies grid refinement leads to better solution accuracy and in some methods different and richer turbulence physics is obtained by using a finer mesh. The turbulence modeling strategy that will be employed is certainly a settlement between the accuracy of the solution and the computational efficiency. Several diferent methods can be used to model turbulent flows such as Direct Numerical Simulation (DNS), Large Eddy Simulation (LES), Detached Eddy Simulation (DES) and models based on Reynolds Averaged Navier-Stokes (RANS) equations.

RANS models are the most frequently used ones by commercial codes. If the turbulent shear stress is defined similar to the laminar shear stress, a new turbulent viscosity called 'eddy viscosity' can be suggested [29]. The eddy viscosity depends on velocity and length scales. In order to define these scales various assumptions and different number of equations are used. In zero-equation models no additional transport equations are used other than mass, energy and momentum equations. In one-equation models turbulent viscosity is described as a function of turbulent kinetic energy. The Spalart-Allmaras model is a one-equation turbulence model. In a two-equation model the main idea is to model turbulent kinetic energy, k, and energy dissipation rate, ω. The most popular two-equation models are k-omega $(k-\omega)$, and k-epsilon $(k-\varepsilon)$, models $(\varepsilon = k^n\omega^m)$. RANS models are not accurate enough to successfully predict the instantaneous dynamic flow behavior due to their time average nature. URANS, which is the unsteady RANS solution method, can be used for transient unsteady solution but it is not available in ADINA-CFD. Therefore, RANS method is not used in our numerical solutions.

3.3.1. Detached Eddy Simulation (DES)

DES is a hybrid method between RANS and LES. It is a three dimensional unsteady numerical solution that uses a single turbulence model. DES functions in such a way that LES is used in regions where the mesh density is fine enough. RANS solution is performed for regions near solid boundaries and regions with not enough mesh points.

A formulation is proposed based on the one-equation Spalart-Allmaras RANS model [32], in which the distance to the closest wall, d, is used as a length scale [33]. In DES approach, the distance d is replaced in the equations by a new length scale parameter $\tilde{d}$. The new length scale parameter $\tilde{d}$ depends on the grid spacing Δ,

$$\tilde{d} \equiv \min(d, C_{DES}\Delta) \tag{3.11}$$

where Δ is the largest dimension of the grid cell.

$$\Delta \equiv \max(\Delta x, \Delta y, \Delta z) \tag{3.12}$$

Here, it is assumed that the grid is structured and x, y and z coordinates are aligned according to the grid cell. If the grid cell is unstructured, then largest dimension of the grid cell can be taken as the diameter of the grid divided by $\sqrt{3}$ [34]. C_{DES} is an empirical constant and assigned to 0.65; and it is not very critical [33].

3.3.2. Large Eddy Simulation (LES)

Spatially coherent structures which change and develop in time are called as eddies. The largest eddies in flow have dynamic and geometric properties related with the mean fluid flow and larger eddies have more energy than the smallest eddies. The LES model is a spatial filtering approach, as the large eddies are numerically simulated but the smallest eddies are modeled. Large eddy and small eddy structures are shown in Figure 3.2. In LES approach, Navier-Stokes equations are solved for a range of length scales. Time dependent equations are solved for large scale motions, therefore the computational cost is reduced when compared with DNS. By this way, simulation of the smallest eddies are eliminated and when compared with DNS, the solution time is shortened.

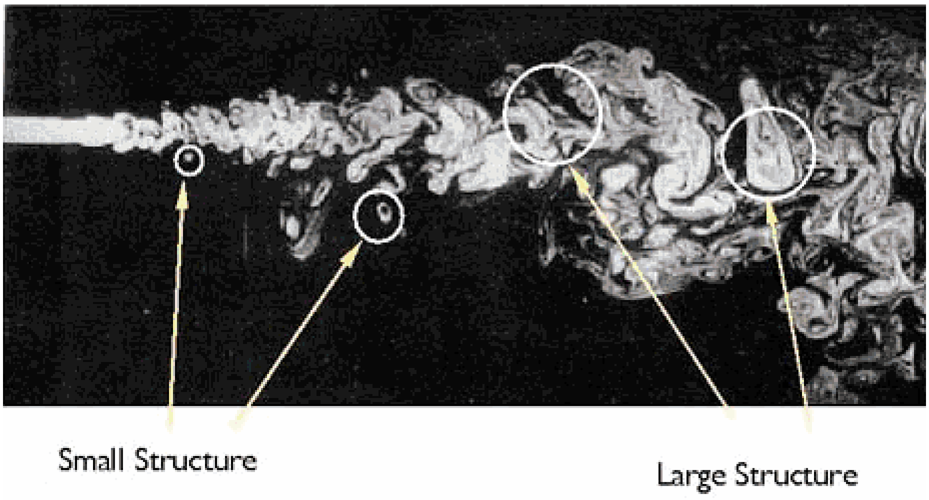

Figure 3.2 Eddy structures [19]

The small scale eddies that can not be solved by the mesh is approximated by an appropriate method referred as 'subgrid-scale-model'. Most of the energy is carried by larger eddies and the current computing power is sufficient to solve time dependent equations for these eddies. Subgrid-scale-model depends on the fact that the turbulence dissipation level is set by the largest eddies and smaller eddies display a similar behavior while transmitting energy to the smallest scales [35]. However, boundary-layer grids should be fine enough to capture the near-wall eddies [36]. The large scales are separated from small scales by performing spatial filtering,

$$\bar{f}(\vec{x}) = \int f(x')G\left(\vec{x} - \vec{x'}; \Delta\right) dx', \tag{3.13}$$

where G is the filter function and Δ is the filter width.

Several subgrid scale models are developed including Smagorinsky model, scale similarity models, renormalization group models (RNG) and dynamic subgrid scale models [37]. One of the most commonly used subgrid scale model based on eddy-viscosity approach is Smagorinsky model, in which the length scale is defined by,

$$l = C_s\Delta \tag{3.14}$$

where C_S is the Smagorinsky constant and Δ is the width of the filter. In this method it is assumed that energy production and dissipation of the small scales are in equilibrium. In other words, the velocity scale is obtained by assuming energy obtained from the larger scales is instantaneously dissipated to smaller scales completely [36].

3.3.3. Direct Numerical Simulation (DNS)

In DNS, the entire range of turbulent scales are resolved and there is not any empiricism. The Navier-Stokes equations are solved without any modeling. In order to resolve all scales of turbulence, a high grid requirement is necessary. The grids should be fine enough to capture the smallest scales and the problem domain should be large enough to contain an adequate sample of the largest eddies [36]. A three-dimensional DNS requires a number of mesh points N^3 satisfying,

$$N^3 \geq Re^{9/4}. \tag{3.15}$$

The number of required mesh points to perform DNS are nearly 6×10^6 and 27×10^6 for Reynolds numbers 1000 and 2000 respectively. For higher Reynolds numbers, more computational power is needed. Also incremental time step has an importance. The integration of solution must be performed by employing a time step Δt, which is small enough that a fluid particle should move only a fraction of the grid spacing Δx, in each time step [36]. In our numerical simulations DNS is not used due to the excessive computational cost.

3.4. Model Geometry

Yazicioglu et al. investigated acoustic radiation from a fluid filled tube experimentally, measured the wall pressure fluctuations and vibrations of the structure for Reynolds numbers 1000 and 2000 [21]. In our work, the geometry and flow conditions of the experimental study in [21] are used for the numerical simulations and the results of numerical simulations are compared with the results found in literature as presented in Chapter 4.

The geometry of flow is cylindrical and axisymmetric as seen in Figure 3.3. There is a constriction in the geometry which represents the severe stenosis. The percent reduction of flow area which is caused by the constriction is obtained by

$$S = \left(\frac{D^2 - d^2}{D^2}\right) \cdot 100\ \% \tag{3.16}$$

where S is the severity of the constriction, d is the constricted diameter and D is the diameter when there is no constriction. In [21] the unconstricted diameter is $6.4\ mm$ where the constricted diameter is $2.3\ mm$ with a blunt form, which leads 87% flow area reduction.

The velocity of the flow is increased sharply near the constricted area. Mean flow velocity at the constriction can be obtained by,

$$U_t = U\left(\frac{D}{d}\right)^2 \tag{3.17}$$

where U_t is the mean velocity at the throat of stenosis and U is the mean velocity at the inlet of the flow. In the experimental study [21] inlet flow conditions are controlled and Reynolds number is calculated at the inlet of the flow domain. The Reynolds number at the inlet of the flow is obtained by,

$$Re_D = U\frac{D}{\nu}, \tag{3.18}$$

where,

$$\nu = \frac{\mu}{\rho}. \tag{3.19}$$

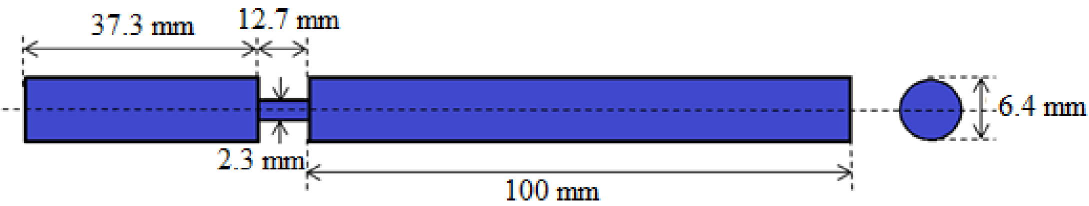

Figure 3.3 Cross-sectional view of the flow domain

Numerical simulations are performed for three different cases. In the first case, the vessel is assumed as rigid, thus the vessel wall does not make any movement and no vibration is present. No slip boundary condition is used for the fluid at the vessel wall and there is no need to model structure for rigid wall assumption. A prescribed uniform velocity profile is introduced at the inlet of the fluid domain. The pressure at the outlet of the fluid domain is set as zero. ADINA-CFD module is used to model the rigid wall problem. Nodal pressures at the wall are recorded and as the results will be presented and discussed in Chapter 4, it is found that the nodal pressures at the wall are fluctuating.

After completing the rigid walled simulations, the fluid filled vessel structure is modeled by using ADINA-Structures. The vessel has $100\,mm$ length and $0.3\,mm$ thickness. The structure covers the $100\,mm$ length downstream region of flow as represented in Figure 3.4. Modal analysis is carried on for this compliant structure. The natural frequencies and mode shapes are determined for the compliant structure by using ADINA-Structures module.

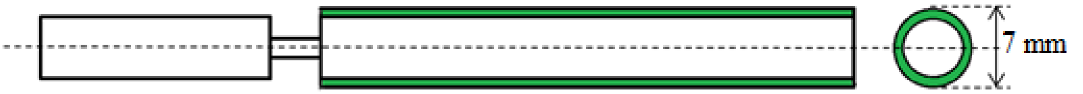

Figure 3.4 Cross-sectional view of the structure covering the downstream of the flow

Lastly, the fluid filled compliant structure is coupled with the flow domain. The compliant structure geometry vibrates due to the flow conditions. The FSI model is defined and solved by using ADINA-FSI module. The red line in Figure 3.5, represents the FSI boundary.

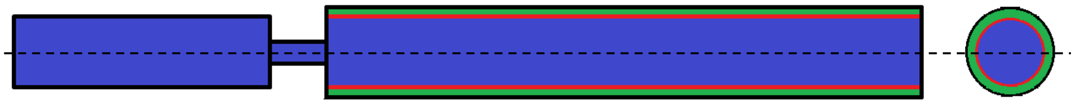

Figure 3.5 Cross-sectional view of flow domain with FSI

3.5. Model Parameters

Larger blood vessels have inner diameters in the range $1 - 20\,mm$, wall thickness diameter ratio of $0.04 - 0.13$ and these vessels can be modeled as thin-walled elastic structures [38, 8, 16, 17, 39, 40]. In FSI simulations, vessel material properties are modeled by using the properties of latex rubber material. In Table 3.1, the comparison between the parameters of larger blood vessels and the parameters of the structure model is represented.

Table 3.1 Parameters of latex vessel (A) and larger blood vessel (B), D is inner diameter, h is wall thickness, E is Young's modulus, ρ is mass density, ν is Poisson's ratio [16]

	D, (mm)	h, (mm)	h/D	E, (N/m^2)	ρ, (kg/m^3)	ν
(A)	6.4	0.3	0.0406	$8 \cdot 10^5$	1086	0.495
(B)	1-20	0.04-2.6	0.04-0.13	$(1.29\text{-}10) \cdot 10^5$	690-1350	0.23-0.57

Inner diameter of the vessel is $6.4\,mm$ and the thickness of the latex vessel is $0.3\,mm$. The corresponding thickness diameter ratio for our model is 0.0406 and it is within the biological ranges. As can be seen from Table 3.1, latex material properties are in the range defined for large blood vessel models. Therefore using latex properties for structure model is appropriate for modeling large blood vessel. Latex material is also used in other experimental studies in literature [21, 22].

Water properties at indoor temperature are used for the fluid model. Water is used as fluid instead of blood for in vitro experiments since the properties of water at indoor temperature are similar to properties of blood. Mass density of normal blood is $1050\,kg/m^3$ which is close to mass density of water [7, 38, 8]. In simulations, the mass density and viscosity of water is modeled as $1000\,kg/m^3$ and $0.001\,Pa \cdot s$ respectively.

In numerical simulations, quasi-steady flow is considered. In other words, the pulsatile nature of the blood flow is neglected. The reason for neglecting pulsatile nature is the difference of the frequencies of the cardiac cycle and expected flow parameter fluctuations. The cardiac cycle and the blood flow rate has a frequency in the order of $1\,Hz$. However, the frequencies of the wall pressure fluctuations are in the range of $20 - 1000\ Hz$ [7]. Therefore the cardiac cycle can be thought as a slowly changing function when compared with the pressure fluctuations present due to the stenosis. We considered a certain instant for flow variables which means the pulsatile nature of the cardiovascular system is neglected.

Two different Reynolds numbers are used for the numerical simulations which are 1000 and 2000. These Reynolds numbers are also used in relevant experimental studies for stenosed flows [21]. In larger blood vessels and in arteries such as the ascending aorta, and the carotid and femoral arteries in human body, typically the Reynolds number of the blood flow do not exceed 7000 [38, 8, 17, 22, 41, 42]. Therefore Reynolds numbers of 1000 and 2000 are appropriate for modeling blood flow in larger blood vessels.

The constricted area represents a severe stenosis which changes the laminar flow characteristics to turbulent flow characteristics. Therefore turbulence models are used in the simulations. In the experimental study [21], any information related with the turbulence intensity value is not provided. The recommended turbulence intensity value by ADINA is within 0.01 ~ 0.1. In our simulations, a turbulence intensity value of 0.025 (2.5 %) is used. DES and LES are performed for determining turbulence induced wall vibrations. DES option is only available with Spalart-Allmaras turbulence model in ADINA. Therefore one-equation Spalart-Allmaras turbulence model is used for DES. Results of LES and DES are presented and compared in Chapter 4.

3.5.1. Model Versions

All of the simulations performed are listed in the Tables 3.2, 3.3 and 3.4. In Table 3.2, the list of simulations by using rigid wall assumption is represented. Flow mesh 1, flow mesh 2 and flow mesh 3 are the mesh types created with different mesh densities. These mesh types are used for models with rigid wall assumption and FSI analysis. Structure mesh 1 is created for modeling the fluid filled vessel. Structure mesh 1 contains solid elements for modeling the vessel and fluid elements for modeling fluid inside the vessel. Structure mesh 1 is used for modal analysis and FSI analysis. For FSI analysis, structure mesh 1 is coupled with flow mesh 2. The details of the models and created mesh types are explained in Appendix A.

Table 3.2 Simulations performed with rigid wall assumption

Model Version	Reynolds Number	Turbulence Model	Mesh Type	Flow Assumption
1	1000	DES	Flow mesh	Rigid wall
2	1000	DES	Flow mesh	Rigid wall
3	1000	DES	Flow mesh	Rigid wall
4	2000	DES	Flow mesh	Rigid wall
5	2000	DES	Flow mesh	Rigid wall
6	2000	DES	Flow mesh	Rigid wall
7	1000	LES	Flow mesh	Rigid wall
8	1000	LES	Flow mesh	Rigid wall
9	1000	LES	Flow mesh	Rigid wall
10	2000	LES	Flow mesh	Rigid wall
11	2000	LES	Flow mesh	Rigid wall
12	2000	LES	Flow mesh	Rigid wall

In Tables 3.3 and 3.4, the list of simulations of modal analysis and FSI models are represented, respectively.

Table 3.3 List of simulations of modal analysis

Model Version	Analysis Type	Mesh Type
13	Modal analysis	Structure mesh 1

Table 3.4 List of FSI simulations

Model Version	Reynolds Number	Mesh Type	Turbulence Model	Analysis Type
14	1000	Structure mesh 1 + Flow mesh 2	DES	FSI
15	2000	Structure mesh 1 + Flow mesh 2	DES	FSI
16	1000	Structure mesh 1 + Flow mesh 2	LES	FSI
17	2000	Structure mesh 1 + Flow mesh 2	LES	FSI

CHAPTER 4

RESULTS AND DISCUSSION

In this chapter the results of numerical simulations are presented and compared with the results in literature. The results are presented in three parts. In the first part the results of models with rigid wall assumption are presented. Secondly, the modal analysis results of the fluid filled tubular structure are presented and lastly the results of FSI analyses are discussed.

4.1. Results of Numerical Simulations with Rigid Wall Assumption

As a first approximation, the tubular structure which covers the flow domain is assumed as a rigid body. Therefore, the geometrical form of the flow domain does not change and the tubular structure does not have any motion. In this way, it is possible to concentrate solely on the fluidic problem. CFD analyses are conducted in order to find the mean velocity distributions, pressure distributions and fluctuating wall pressures on the wall boundaries downstream of constriction exit. As mentioned previously in Chapter 3, three different mesh types are used for CFD analyses. These mesh types have different mesh densities. Flow mesh 1, flow mesh 2 and flow mesh 3 contain elements around 80000, 150000 and 300000 respectively. The CFD analyses results of three different mesh types are compared. The element sizes of the flow meshes are limited due to using only a single computer for numerical simulations.

Durations to complete the CFD analyses are represented in Table 4.1. CFD analyses are performed for both DES and LES models. As mentioned earlier in Chapter 3, DES is a hybrid model between LES and RANS methods.

Table 4.1 Durations of CFD analyses on a single PC (Intel Core i7 processor with 6GB RAM running Windows 7)

Type of Mesh and Flow Model	$Re_D = 1000$	$Re_D = 2000$
Flow mesh 1 – DES	About 16 hours	About 19 hours
Flow mesh 1 – LES	About 16 hours	About 20 hours
Flow mesh 2 – DES	About 36 hours	About 46 hours
Flow mesh 2 – LES	About 36 hours	About 48 hours
Flow mesh 3 – DES	About 71 hours	About 86 hours
Flow mesh 3 – LES	About 73 hours	About 90 hours

As seen in Table 4.1, durations of numerical simulations increase for denser mesh types. In the numerical analyses the flow is simulated for 4600 time steps. First 100 steps are performed with a time step of 0.01 seconds and then 4500 steps are perfomed with a time step of 1/4096 seconds. This time step is selected identical to the sample rate used in the instrumentation of the experiments by Yazicioglu et al. [21] to match the parameters used in the spectral calculations. In the first 100 time steps mean flow parameters reach a quasi-steady value. The durations for DES and

LES models are nearly the same and the difference is not critical. As the Reynolds number of the flow increase, durations of the numerical simulations also increase.

4.1.1. Acoustic Pressures for Rigid Wall Assumption Models

The mean wall pressures reach a quasi-steady value but there are low amplitude fluctuations on top of the mean dynamic pressure. As an example, the pressure-time history of a fluid node placed on the wall is shown in Figure 4.1.

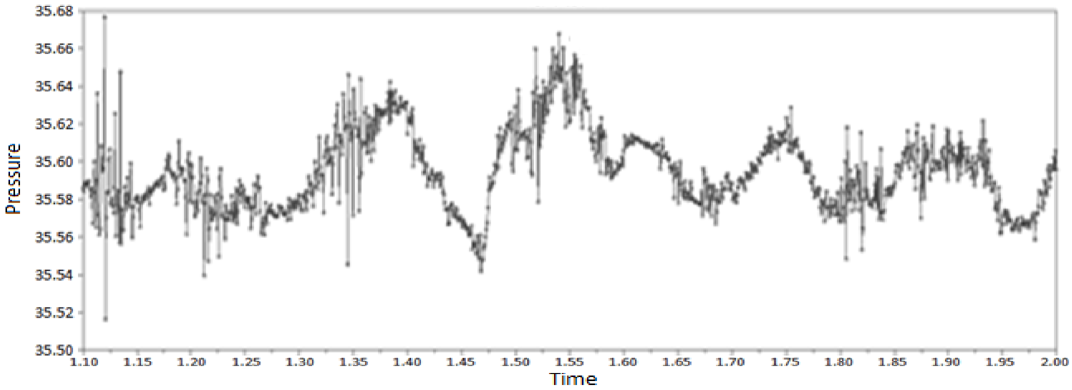

Figure 4.1 Time history of pressure of a node placed on the wall (Pa, s)

The time history of pressure data is recorded for the nodes placed on the wall for 100 mm downstream of the constriction exit. The frequential distribution of the wall pressure fluctuations are obtained by using last 4096 data points from the pressure time data. Hanning window is used to select a subset of samples for performing a Fourier transform. In order to monitor the spectral behavior of the fluctuating pressures on the wall, Fast Fourier Transform (FFT) is performed on the pressure data by MATLAB (code is available in Appendix B). Acoustic pressure amplitudes are represented in logarithmic scale by using the equation,

$$p(dB) = 20 \cdot log_{10}\left(\frac{p(Pa)}{p(Ref)}\right) \tag{4.1}$$

where $p(dB)$ is the acoustic pressure amplitudes in dB, $p(Pa)$ is the pressure amplitudes in Pa which is obtained from numerical simulations and $p(Ref)$ is reference pressure in Pa. The acoustic pressures obtained by using flow mesh 1, flow mesh 2 and flow mesh 3 are shown in Figures 4.2, 4.3 and 4.4 respectively.

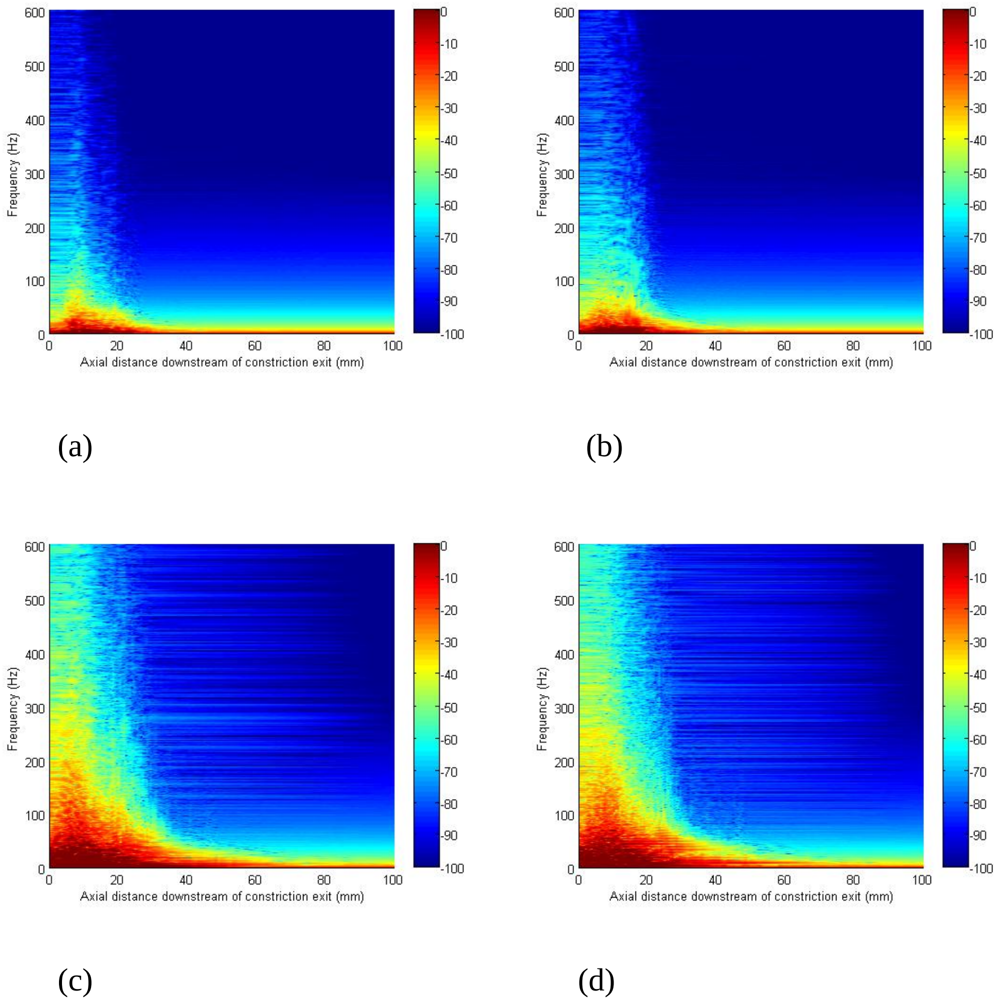

Figure 4.2 Acoustic pressure (dB *re*: 1 Pa) near wall inner surface as function of axial position and frequency by using flow mesh 1. All cases are for a rigid tube with a constriction ending at 0 mm. (a) DES, $Re_D = 1000$. (b) LES, $Re_D = 1000$. (c) DES, $Re_D = 2000$. (d) LES, $Re_D = 2000$.

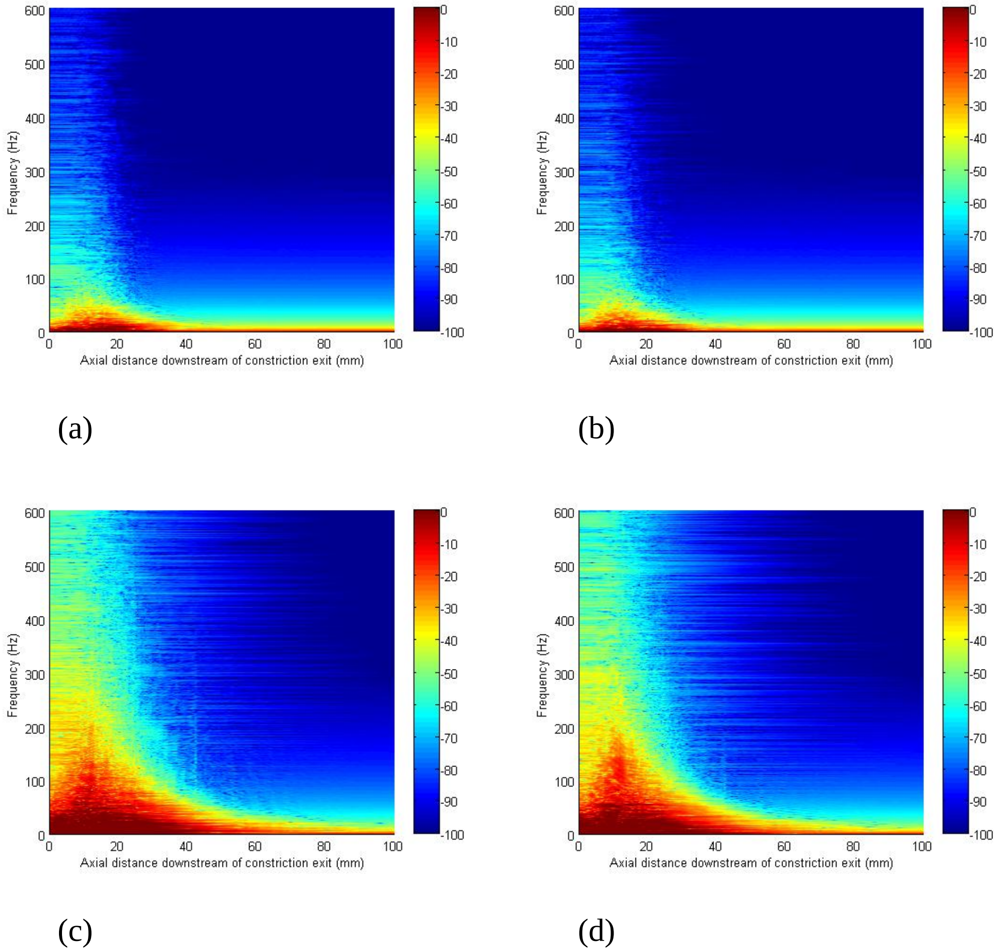

Figure 4.3 Acoustic pressure (dB *re*: 1 Pa) near wall inner surface as function of axial position and frequency by using flow mesh 2. All cases are for a rigid tube with a constriction ending at 0 mm. (a) DES, $Re_D = 1000$. (b) LES, $Re_D = 1000$. (c) DES, $Re_D = 2000$. (d) LES, $Re_D = 2000$.

.

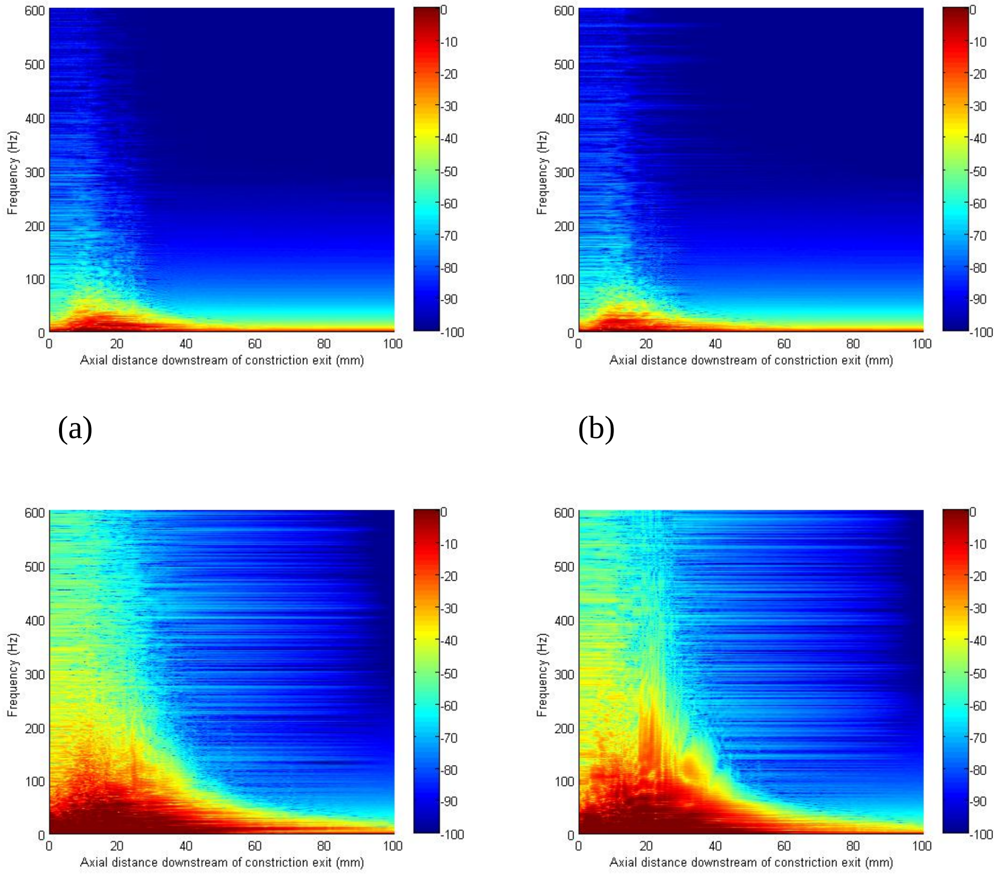

(a) (b)

(c) (d)

Figure 4.4 Acoustic pressure (dB *re*: 1 Pa) near wall inner surface as function of axial position and frequency by using flow mesh 3. All cases are for a rigid tube with a constriction ending at 0 mm. (a) DES, $Re_D = 1000$. (b) LES, $Re_D = 1000$. (c) DES, $Re_D = 2000$. (d) LES, $Re_D = 2000$.

By using three flow mesh types, similar results are obtained for DES and LES models. As seen in Figures 4.2, 4.3 and 4.4, there is significant information in the frequency spectrum of the wall pressure signal. In Figure 4.5, acoustic pressures at $f = 100\ Hz$ are compared for three mesh types by using DES model.

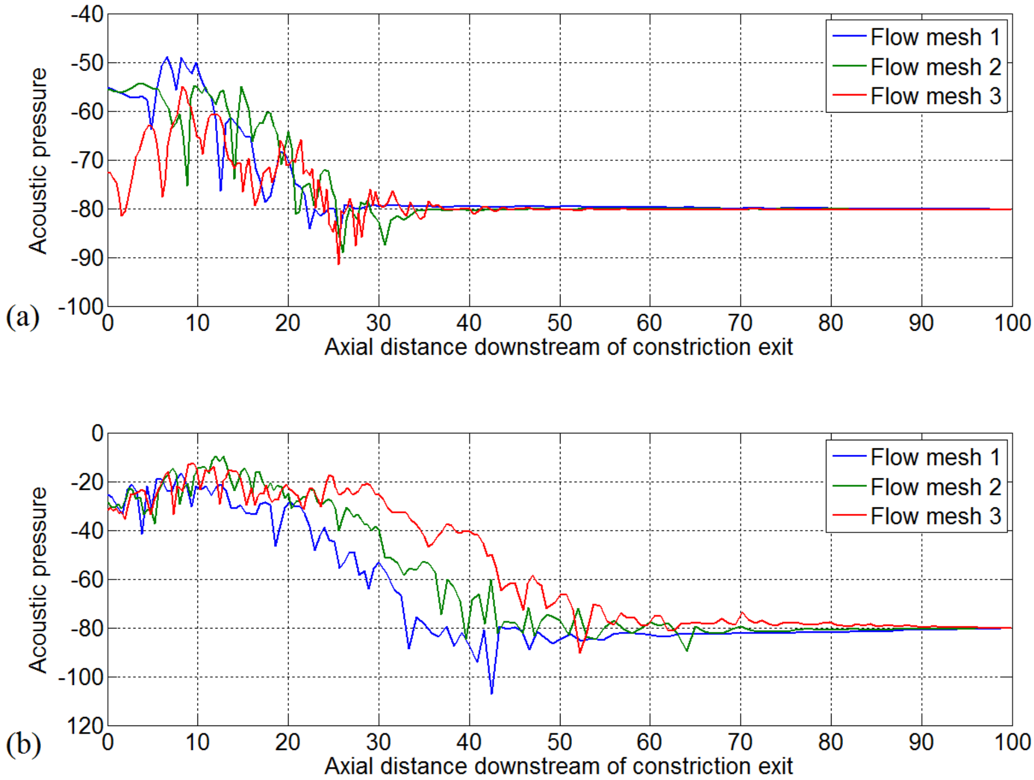

Figure 4.5 Acoustic Pressure (dB re: 1 Pa) on inner wall surface as function of axial position for $f = 100\ Hz$. All cases are for a rigid tube with a constriction ending at 0 mm. (a) DES, $Re_D = 1000$. (b) DES, $Re_D = 2000$.

As seen in Figure 4.5, an excitation is present in first $30\ mm$ for $Re_D = 1000$. For $Re_D = 2000$ case, as the mesh density becomes higher, amplitudes of acoustic pressures slightly increase between the range of 20-50 mm downstream of constriction exit. The results do not agree perfectly for three flow mesh sizes. By using a finer mesh, more detailed turbulence physics and higher solution accuracy can be obtained. However, we observed agreement in terms of general spectral behavior where the excitation is mostly seen in the first $30\ mm$ and the excitation is increased with higher Reynolds number.

Numerical results display that the dynamic acoustic pressure increases with increasing Reynolds number. The spectral amplitudes of acoustic pressure for $Re_D = 2000$ are higher than those of $Re_D = 1000$. For the first 30 mm from the constriction exit which is the recirculation region, the amplitudes of acoustic pressures are higher when compared with the rest of the downstream region. The most active location within the recirculation region is not just the exit of the constriction but around 10-15 mm downstream of the constriction exit. Also for the recirculation region which is highly disturbed, a wide range of frequencies are excited. The amplitudes of acoustic pressures decrease gradually as the frequency increases. Downstream of the recirculation region, the amplitudes decrease sharply and a narrow band of frequencies are excited.

For the same geometry and flow conditions, Yazicioglu et al. [21] obtained experimental results. The experimental results are shown in Figures 4.6 [21].

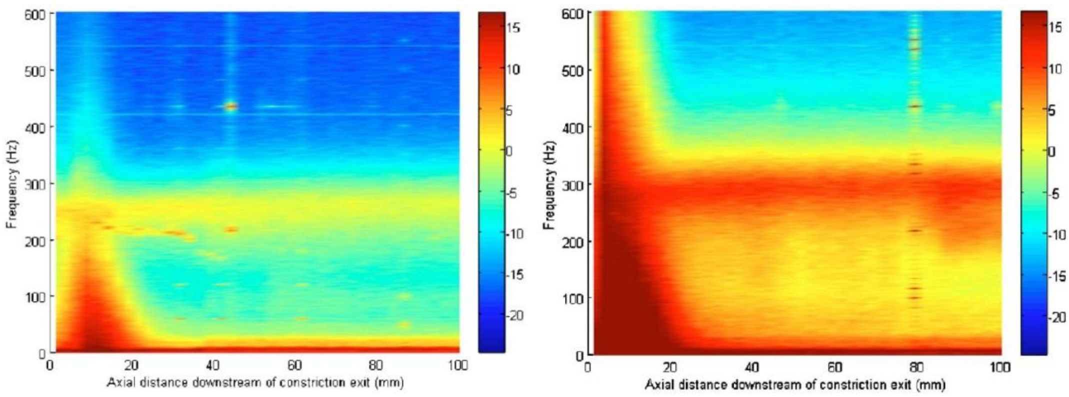

(a) (b)

Figure 4.6 Acoustic pressure (dB *re*: 1 Pa) near wall inner surface as function of axial position and frequency by using experimental results [21]. All cases are for a rigid tube with a constriction ending at 0 mm. (a) Experiment in rigid tube for $Re_D = 1000$. (b) Experiment in rigid tube for $Re_D = 2000$.

It is seen that experimental results display the same spectral character as the numerical ones. However, there is a significant difference in amplitudes. The experimental results have higher acoustic pressure amplitudes. Lee et al. [43] indicated that a reason for the discrepancy of such experimental and numerical results can be quiescent inflow condition used in numerical models. More realistic inflow conditions changing with time can affect the pressure and velocity fluctuations of the flow. Also the excitation present around $300\ Hz$ in experiments, is not observed in our numerical simulations. This excitation may be caused by an acoustic mode of the fluid in the rigid tube which may be damped in the compliant tube. Clearly, as observed in both experimental and numerical results, significant relative increase in dynamic acoustic pressure amplitudes is a sign for presence of a stenosis in vascular flow.

In order to be able to compare the relative amplitudes of the spectral form of pressure more clearly, the data are normalized by using the maximum spectral pressure value in the flow downstream the constriction exit. After this normalization, the maximum acoustic pressure amplitude in the figures will be 0 dB. A MATLAB code is used to display normalized acoustic pressures obtained by numerical simulations (Appendix C). Based on the similarity of spectral character of three meshes, the second mesh with 145872 elements is considered to be good enough. The normalized acoustic pressures obtained by using flow mesh 2 and experimental results [21] are presented in Figure 4.7.

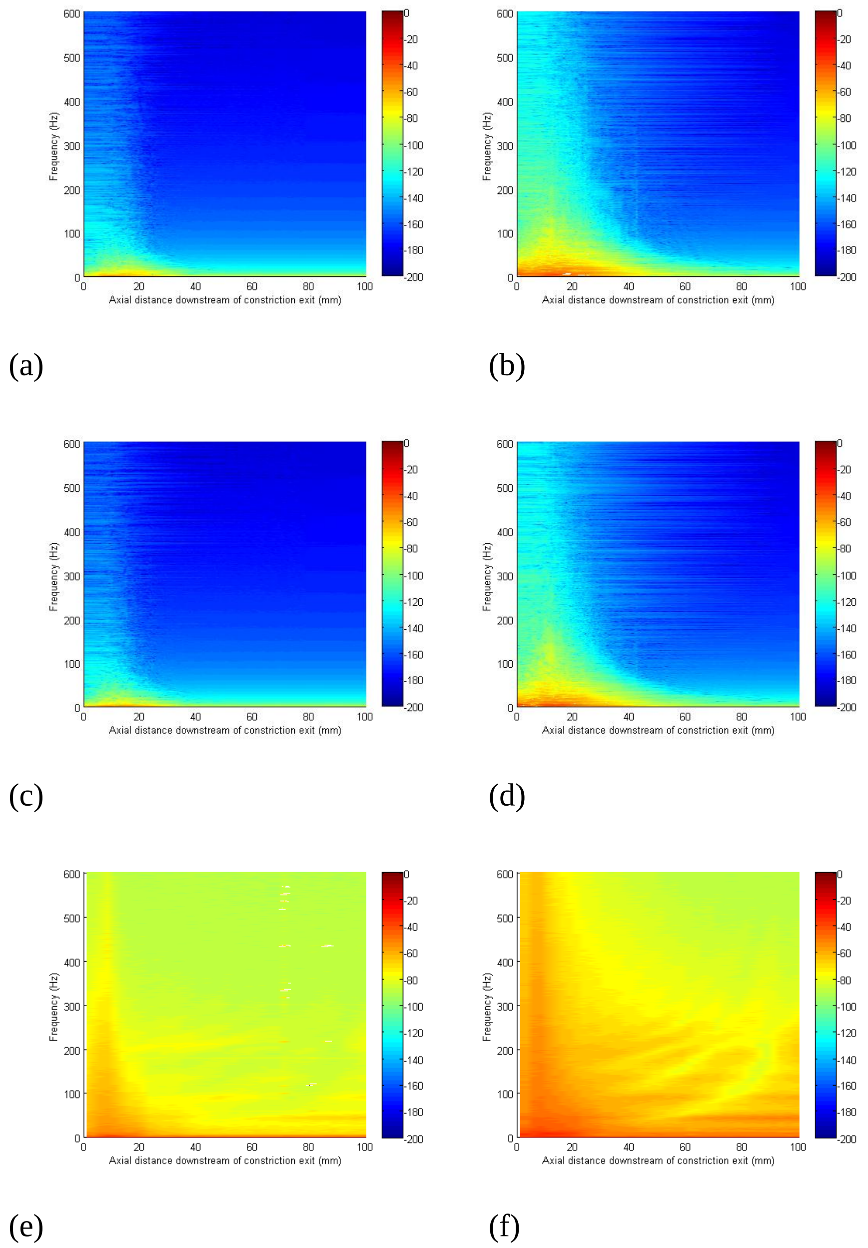

Figure 4.7 Normalized acoustic pressure (dB *re*: Maximum spectral pressure) according to the highest pressure near wall inner surface as function of axial position and frequency by using flow mesh 2. All cases are for a rigid tube with a constriction ending at 0 mm. (a) DES, $Re_D = 1000$. (b) DES, $Re_D = 2000$. (c) LES, $Re_D = 1000$. (d) LES, $Re_D = 2000$. (e) Experiment [21] in rigid tube, $Re_D = 1000$. (f) Experiment [21] in rigid tube, $Re_D = 2000$.

The amplitudes of acoustic pressures decrease gradually for downstream of the constriction exit, however the scaled acoustic pressure amplitudes of numerical simulations decrease more sharply when compared with the scaled amplitudes of the experimental results [21].

4.1.2. Pressure and Axial Velocity Distributions for Rigid Wall Assumption Models

Pressure and axial velocity distributions are obtained by using 3 flow mesh types and nearly the same results are acquired. Instantaneous pressure distributions at $t = 1\ s$, obtained by using flow mesh 2 (145872 elements) are presented in Figure 4.8 and Figure 4.9 for $Re_D = 1000$ and 2000, respectively. Figures 4.8 and 4.9 are the major cross sectional views of the 3-D geometry of flow domain.

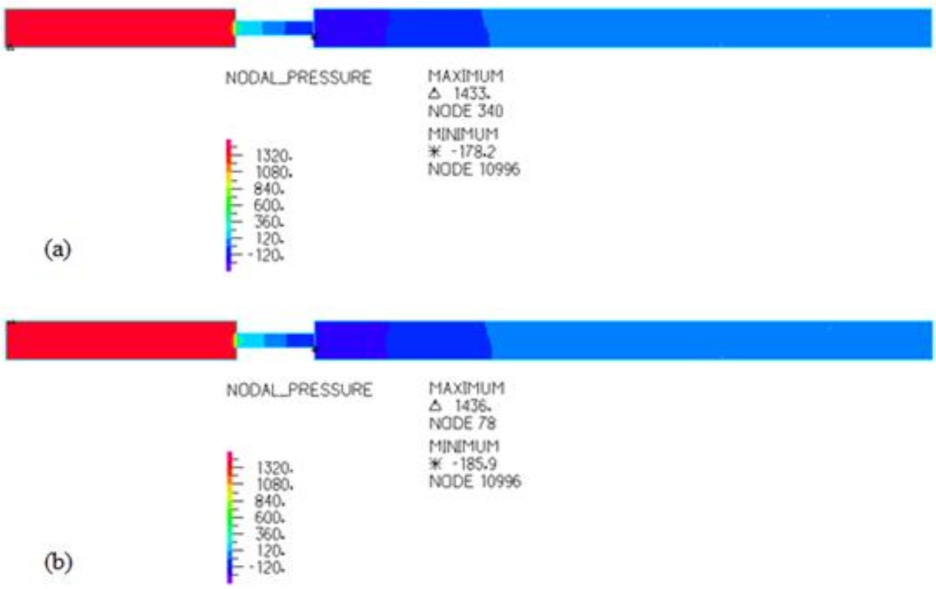

Figure 4.8 Instantaneous pressure (Pa) distribution at $t = 1\ s$, by using flow mesh 2. (a) DES, $Re_D = 1000$. (b) LES, $Re_D = 1000$.

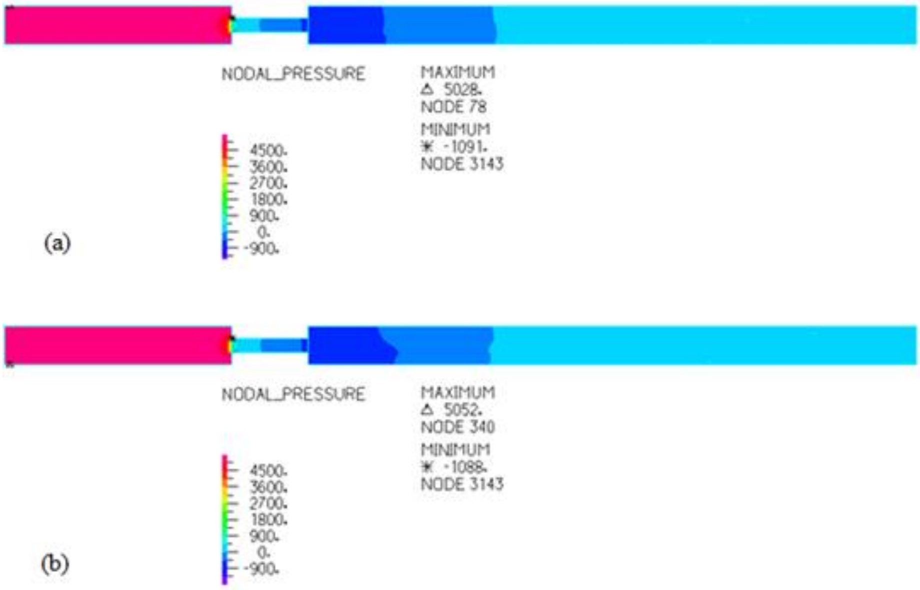

Figure 4.9 Instantaneous pressure (Pa) distribution at $t = 1\ s$, by using flow mesh 2. (a) DES, $Re_D = 2000$. (b) LES, $Re_D = 2000$.

There is an expected pressure drop at the inlet of the constricted area. Then pressure reaches a steady value within 25 mm downstream of the constriction exit and remains nearly constant till the exit of the flow domain. The same behavior is apparent for $Re_D = 1000$ and 2000 but the mean pressure drop (mean pressure difference between exit of constriction and exit of flow domain) is four times higher for $Re_D = 2000$ when compared with the pressure drop for $Re_D = 1000$. The results obtained by using DES and LES models are similar.

Instantaneous axial velocity distributions obtained by using flow mesh 2 are presented in Figures 4.10 and 4.11 for $Re_D = 1000$ and 2000, respectively.

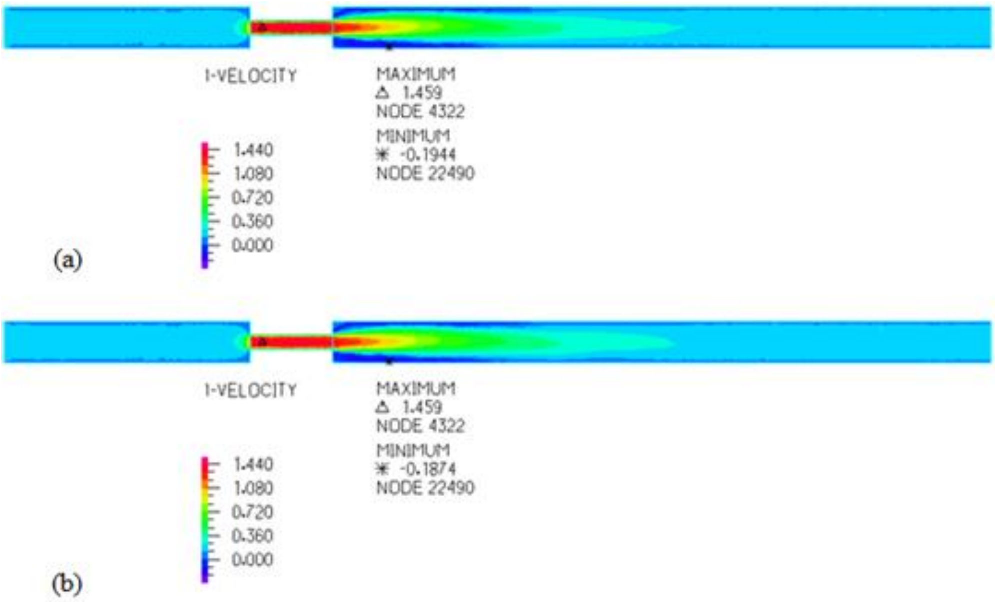

Figure 4.10 Instantaneous axial velocity (m/s) distribution at $t = 1\ s$, by using flow mesh 2. (a) DES, $Re_D = 1000$. (b) LES, $Re_D = 1000$.

The axial velocity of the flow sharply increases at the throat of the stenosis due to the reduction of flow area. At the exit of the stenosis a fluid jet is apparent. The results of the case with $Re_D = 2000$ are more disturbed when compared with $Re_D = 1000$ case. The velocity of the fluid jet increases directly proportional to the Reynolds number, but the length of recirculation region does not change critically. For $Re_D = 2000$, the flow velocity reaches a stable value within 25 mm and does not change significantly till the exit of the flow domain which is similar to the $Re_D = 1000$ case. The results determined by LES and DES models again do not differ and give similar results for velocity profile of flow domain.

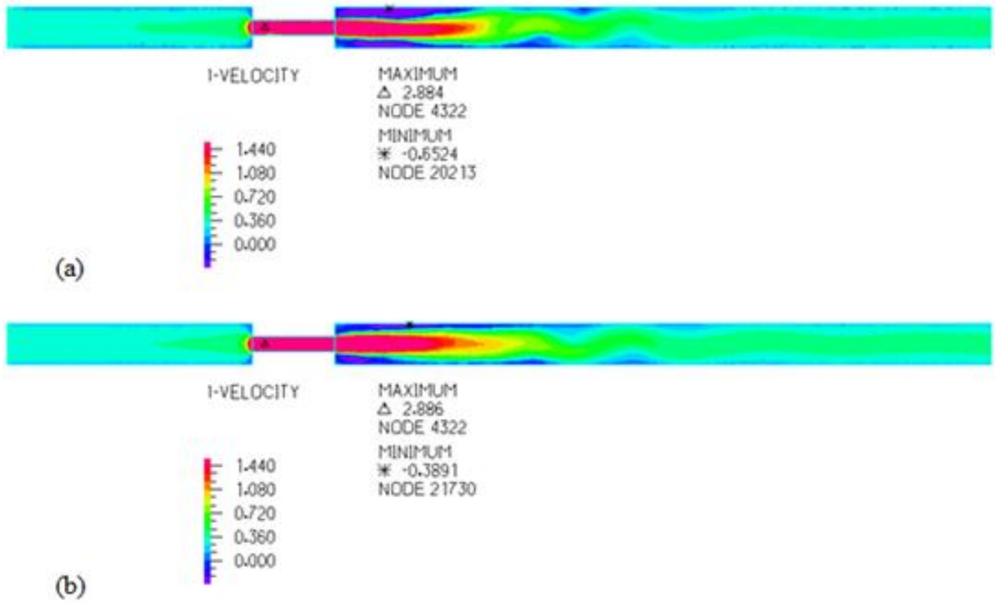

Figure 4.11 Instantaneous axial velocity (m/s) distribution at $t = 1\ s$, by using flow mesh 2. (a) DES, $Re_D = 2000$. (b) LES, $Re_D = 2000$.

Borisyuk also performed experiments about stenosed flows [7]. In Figure 4.12, flow domain is categorized into three different regions. First region is flow separation region and a recirculation zone is apparent in this region. Second region is flow reattachment region and the third region is the flow stabilization and redevelopment region.

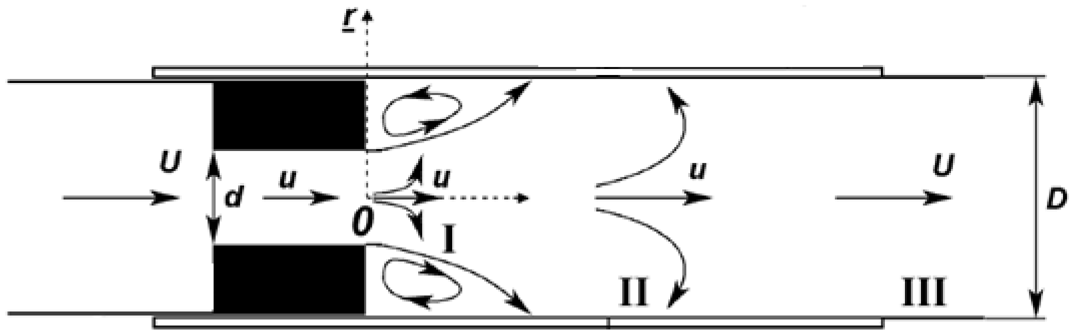

Figure 4.12 Flow regions in the downstream of the constriction exit [7]

The regions shown in Figure 4.12 are also apparent in our numerical simulations. Starting from the exit of the constriction a recirculation region is developed and the length of the recirculation region is similar for $Re_D = 1000$ and 2000. The length of recirculation region for $Re_D = 2000$ is slightly longer when compared with $Re_D = 1000$ case. Tobin and Chang investigated similar flows and developed some universal correlations [22]. In Figure 4.13, the length of recirculation region for different Reynolds numbers is given.

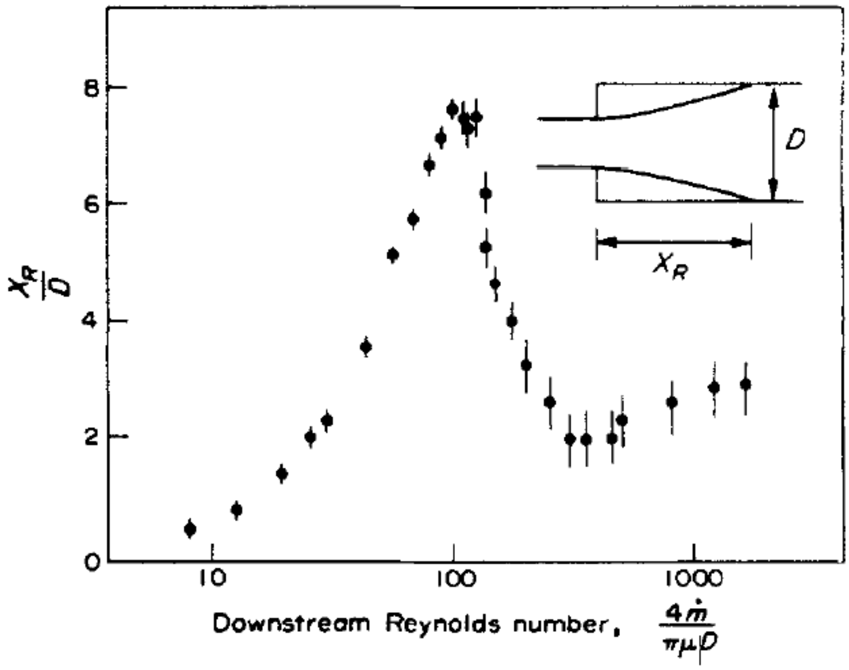

Figure 4.13 Length of recirculation region for Reynolds numbers [22]

In Figure 4.13, X_R is the length of the recirculation region and D is the diameter of the tubular structure. The length of recirculation region for $Re_D = 1000$ can be approximated as $3D$ from Figure 4.13. The length of recirculation region for $Re_D = 2000$ is slightly higher than $3D$.

In Figure 4.14, the length of recirculation region obtained for $Re_D = 1000$ and 2000 by using flow mesh 2 is given. The length of recirculation region is around $3.4D$ and $3.6D$ for $Re_D = 1000$ and 2000, respectively. The length of recirculation region obtained by numerical simulations is slightly higher than $3D$ which is observed by Tobin and Chang [22].

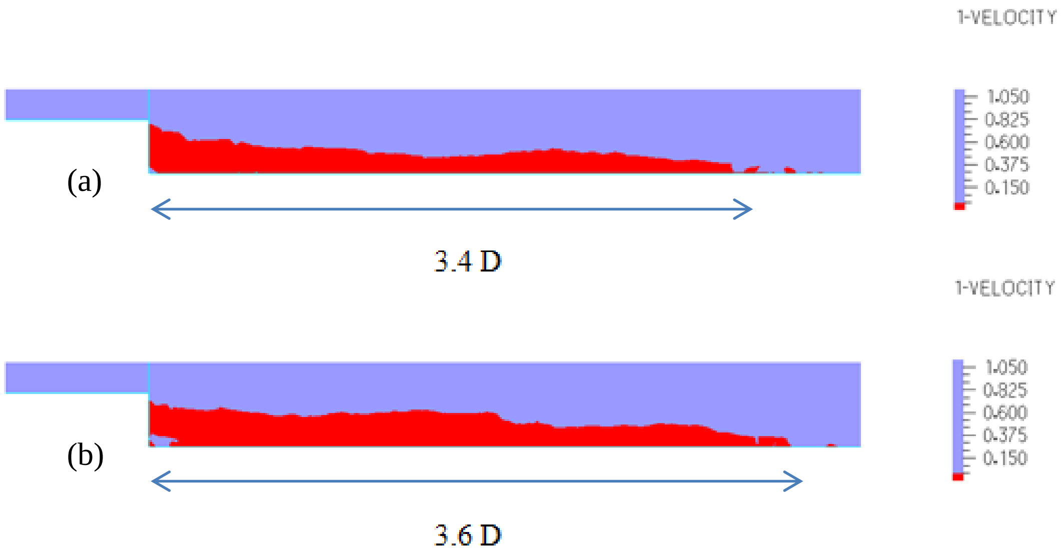

Figure 4.14 Axial velocity (m/s) distribution and length of recirculation region by using flow mesh 2. (a) DES, $Re_D = 1000$. (b) DES, $Re_D = 2000$.

4.1.3. Mean Wall Pressures for Rigid Wall Assumption Models

The geometry of the flow domain is axisymmetric, therefore the wall pressures are recorded for the nodes placed on the $(+z)$ axis which is shown in Figure 4.15.

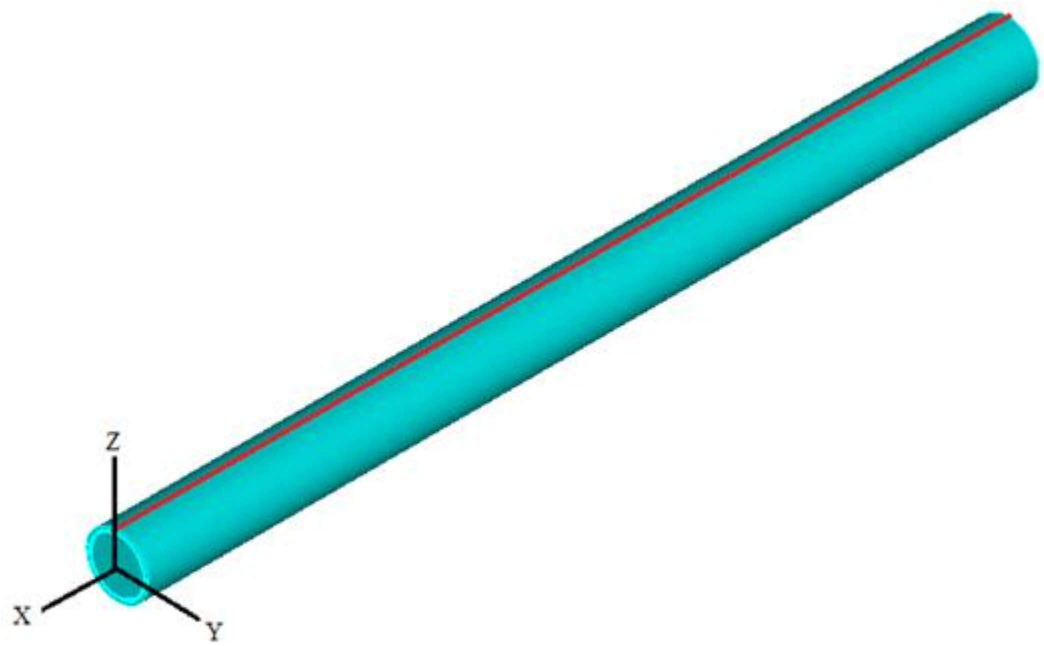

Figure 4.15 Nodes placed on the $(+z)$ axis on the wall

The mean wall pressures changing with the axial distance downstream of constriction exit for DES and LES models are shown in Figures 4.16 and 4.17, respectively. The mean wall pressure at the exit of the flow domain is used as a reference point and taken as zero in the numerical simulations.

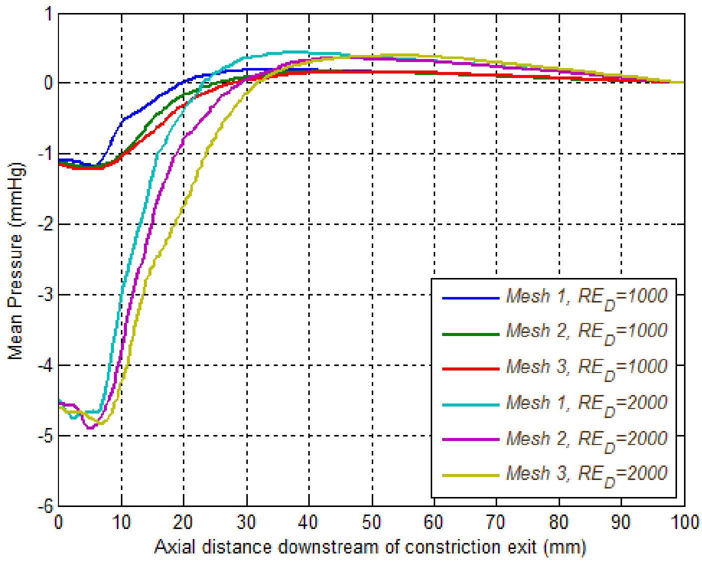

Figure 4.16 Mean wall pressures for three flow mesh types by using DES

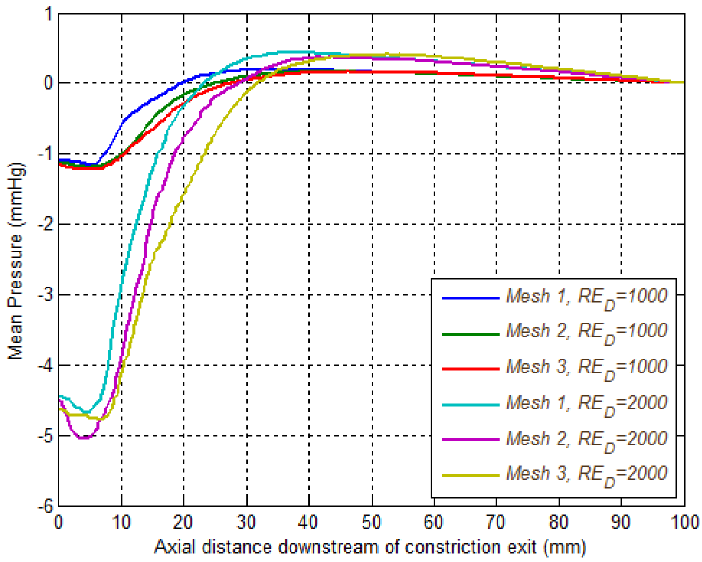

Figure 4.17 Mean wall pressures for three flow mesh types by using LES

The mean wall pressure distributions mostly agree for all three mesh types. There is a wall pressure drop at the exit of the constriction. The wall pressure drop for $Re_D =$ 1000 and 2000 are around 1.25 $mmHg$ and 5 $mmHg$, respectively. The magnitude of mean wall pressure drop increase proportional to the increase in Reynolds number of flow. But the mean wall pressure reaches a stable value within the 20-30 mm distance for both $Re_D = 1000$ and 2000. As can be seen from Figure 4.18, mean wall pressures are nearly the same for DES and LES models.

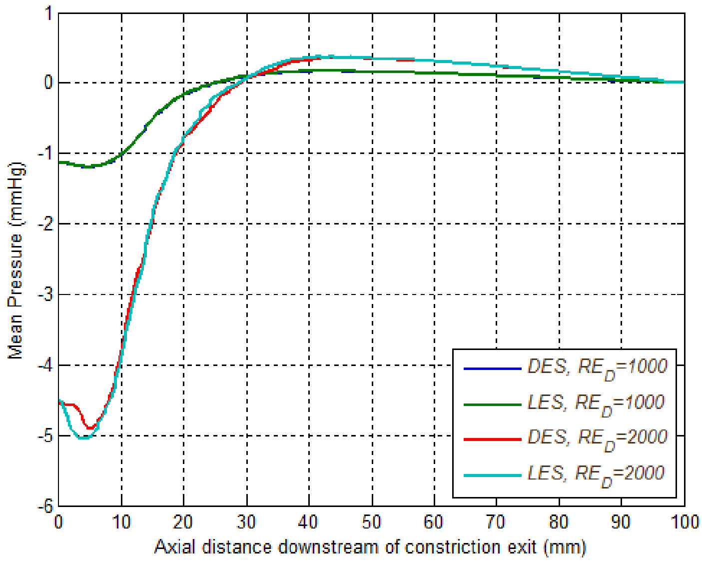

Figure 4.18 Comparison of mean wall pressures for LES and DES by using flow mesh 2

The results of the experimental study [21] is presented in Figure 4.19. The results obtained by experimental study show that when a rigid tube is used, the mean wall pressure drop is around 1.5 $mmHg$ for $Re_D = 1000$. The magnitude of mean wall pressure drop becomes nearly 6 $mmHg$ for $Re_D = 2000$. The mean wall pressure drops obtained by numerical simulations are slightly lower when compared with the experimental results [21].

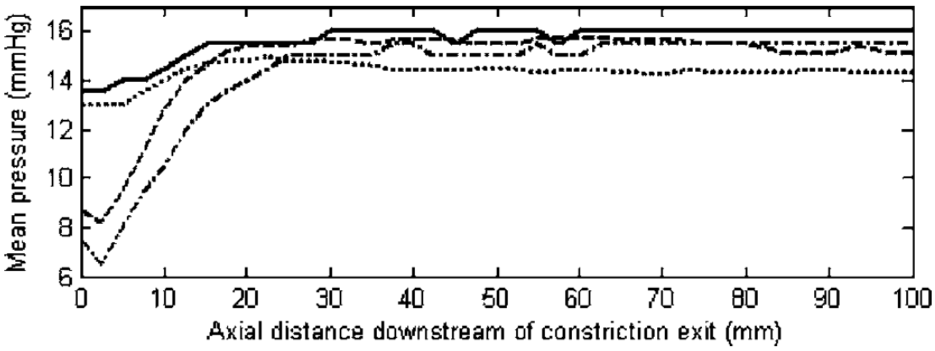

Figure 4.19 Mean pressure obtained by experimental study [21]. Key: ——— $Re_D = 1000$, compliant tube; - - - $Re_D = 1000$, rigid tube; – – – $Re_D = 2000$, compliant tube; – - – $Re_D = 2000$, rigid tube.

For analyses with rigid wall assumption, three flow meshes led to results which are in agreement with each other in terms of mean flow variables. Therefore, for the FSI studies, flow mesh 2, which has the moderate mesh density (145872 elements), is coupled with a compliant tubular structure model.

4.2. Results of Modal Analysis of the Tubular Structure

By using the Structures module of ADINA, the modal analysis of the fluid filled tube is performed. Results for the natural frequencies and mode shapes of the fluid filled tube are shown in Figures 4.20, 4.21, 4.22 and 4.23.

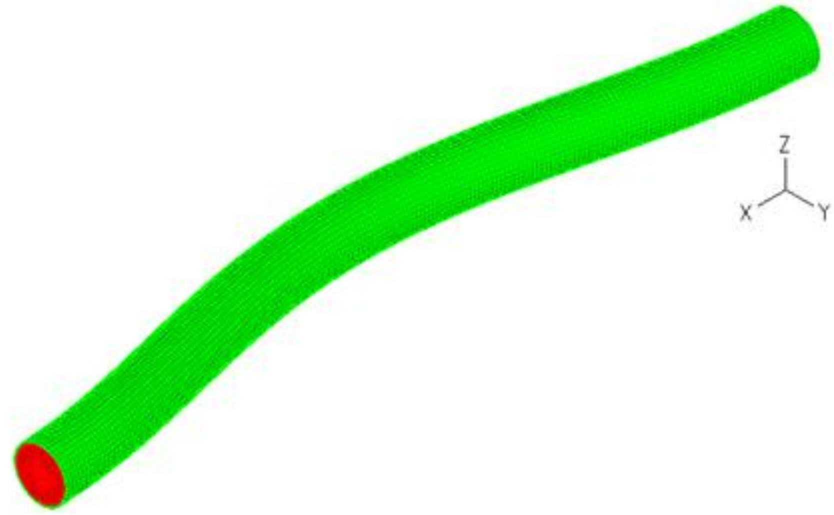

Figure 4.20 First bending mode shape of the fluid-filled compliant tube

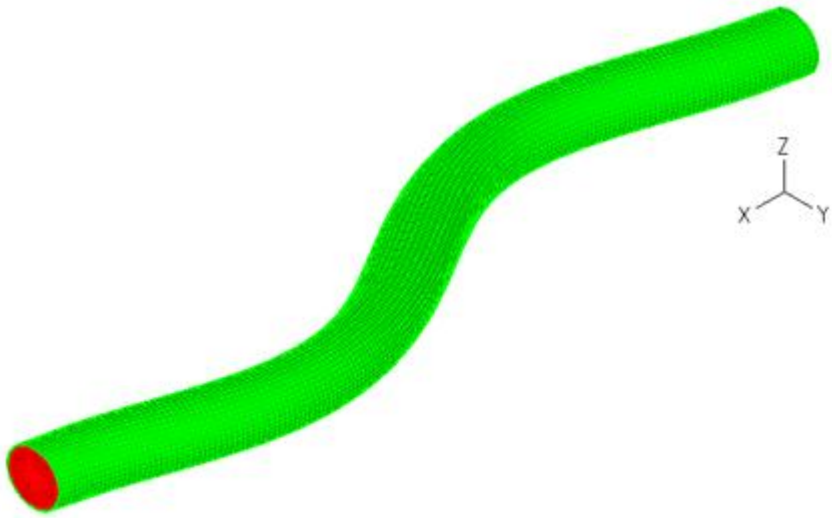

Figure 4.21 Second bending mode shape of the fluid-filled compliant tube

Figure 4.22 First breathing mode shape of the fluid-filled compliant tube

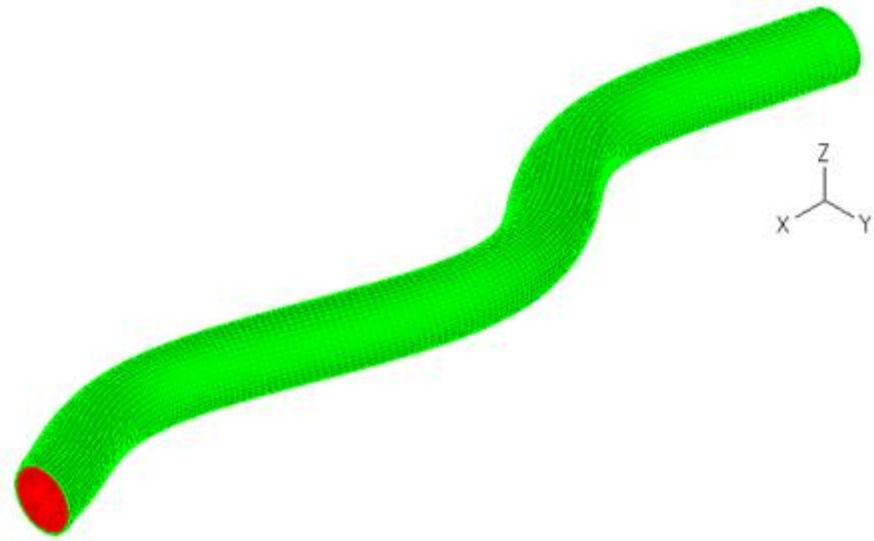

Figure 4.23 Third bending mode shape of the fluid-filled compliant tube

The results of the modal analysis are given in Table 4.2.

Table 4.2 Results of modal analysis

Mode	Modal Analyses
1st Bending Mode	9.04 Hz
2nd Bending Mode	23.30 Hz
1st Breathing Mode	30.61 Hz
3rd Bending Mode	42.45 Hz

4.3. Results of FSI Analyses

In Section 4.1, tubular structure which covers the fluid domain is assumed as a rigid body. In actual case, the blood vessels are compliant, therefore the tubular structure should be modeled as a deformable body. In this section, the tubular structure is modeled as a compliant body and coupled with the fluid model which is previously created in Section 4.1.

4.3.1. Acoustic Pressures for FSI Analyses

The frequency distribution of the acoustic pressures are obtained by performing the same procedure for the rigid wall models. The spectral behavior of acoustic pressures for FSI analyses and experimental results [21] are presented in Figure 4.24.

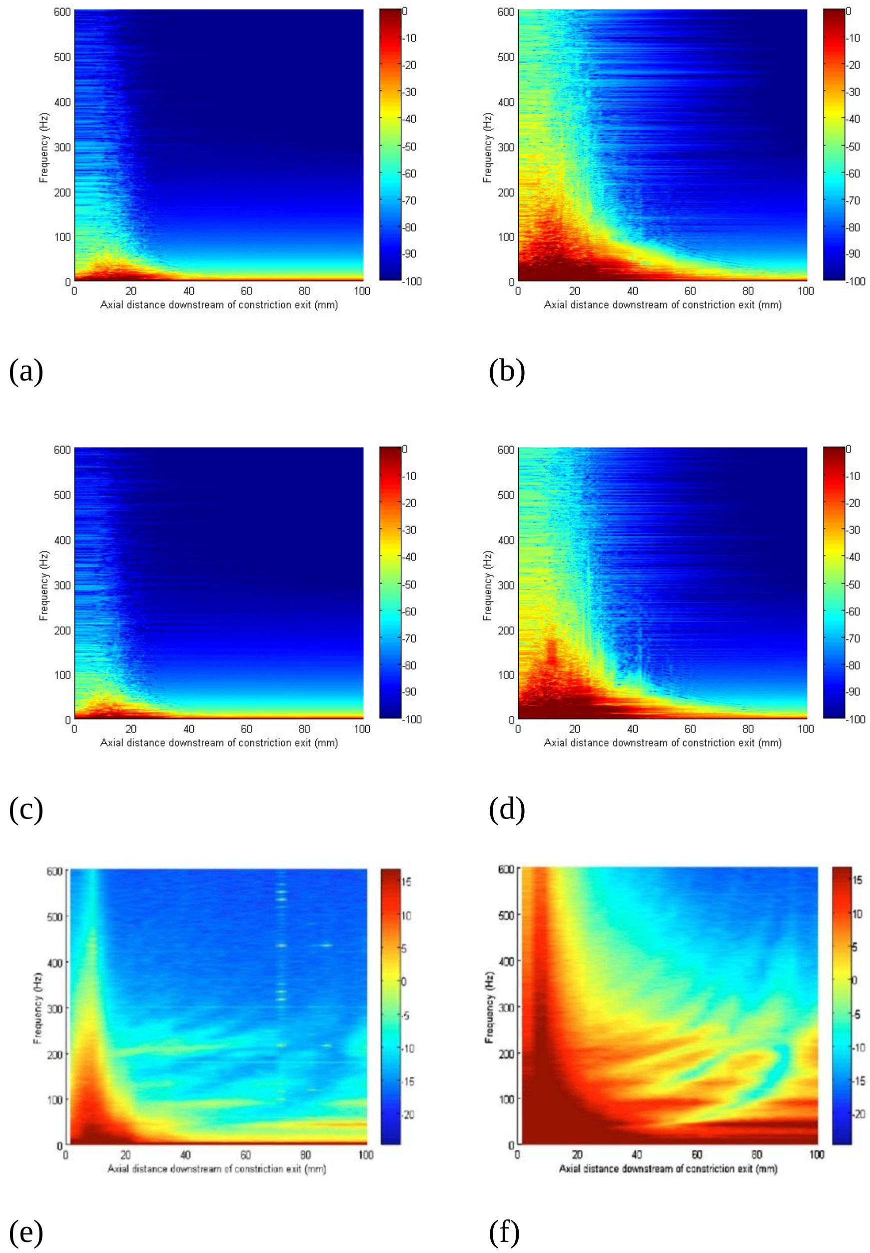

Figure 4.24 Acoustic pressure (dB *re*: 1 Pa) near wall inner surface as function of axial position and frequency by using FSI model (Flow mesh 2 and structure mesh 1 are coupled). All cases are for a compliant tube with a constriction ending at 0 mm. (a) DES, $Re_D = 1000$. (b) DES, $Re_D = 2000$. (c) LES, $Re_D = 1000$. (d) LES, $Re_D = 2000$. (e) Experiment [21] in compliant tube for $Re_D = 1000$. (f) Experiment [21] in compliant tube for $Re_D = 2000$.

The spectral behavior of normalized acoustic pressures for the FSI models is represented in Figure 4.25.

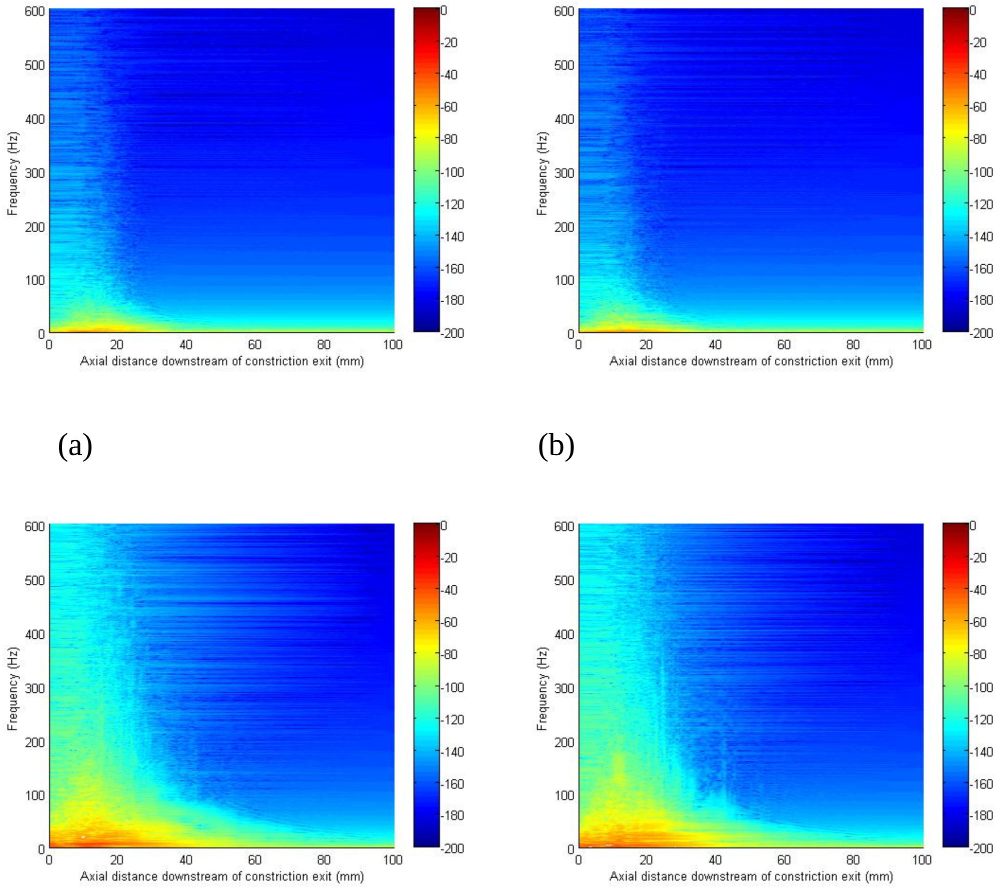

(a) (b)

(c) (d)

Figure 4.25 Normalized acoustic pressure (dB *re*: Maximum spectral pressure) according to the highest pressure near wall inner surface as function of axial position and frequency by using FSI model (Flow mesh 2 and structure mesh 1 are coupled). All cases are for a compliant tube with a constriction ending at 0 mm. (a) DES, $Re_D = 1000$. (b) LES, $Re_D = 1000$. (c) DES, $Re_D = 2000$. (d) LES, $Re_D = 2000$.

It is observed that the dynamic acoustic pressures obtained by FSI simulations are quite similar with the rigid wall assumption models. However, for the experimental studies, it was possible to see the effect of structural response in the pressure signal as seen in Figure 4.24.

A universal parameter which is independent of Reynolds number of the flow and constriction severity is obtained as given in Figure 4.26 [22].

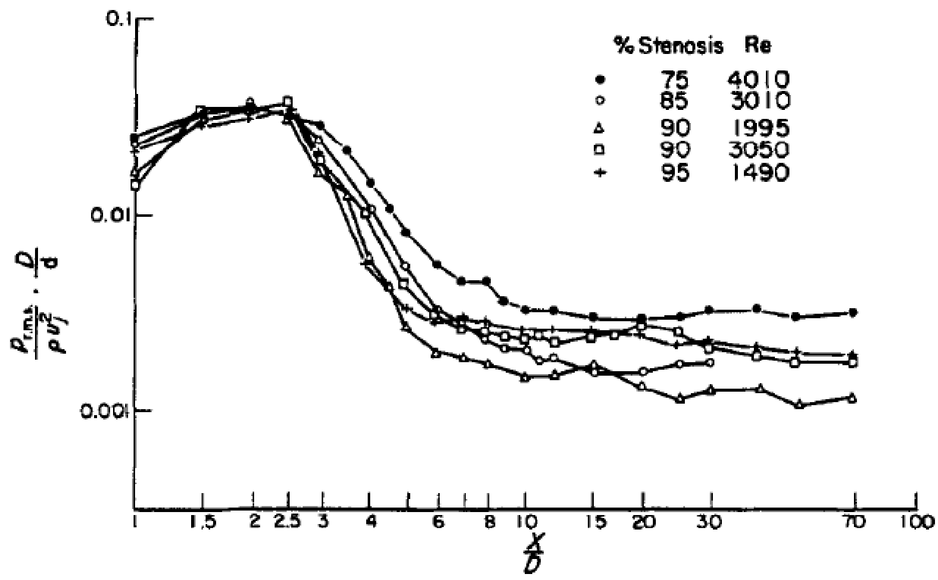

Figure 4.26 Root mean square (R.M.S.) wall pressure variation with x/D, normalized data – assorted Reynolds numbers and degrees of stenosis [22]

In Figure 4.26, x denotes the axial distance downstream of the constriction exit, D is the diameter of the tube, d is the constricted diameter, ρ is the density of the fluid, u_j is the mean velocity at the constricted region and p_{rms} is the root mean square pressure. For flows with different Reynolds numbers and different stenosis degrees, a similar behavior is obtained for the universal parameter

$$\frac{p_{rms}}{\rho u_j^2} \cdot \frac{D}{d} \tag{4.2}$$

as seen in Figure 4.26.

Yazicioglu et al. [21] used the universal parameter obtained by Tobin and Chang [22] and used the following equation to find the time history of the wall pressure amplitudes for different Reynolds numbers and stenosis degrees,

$$p[x] = 1.82 F_{n1}[x/D] \rho U^{3/2} \cdot \frac{D^{5/2}}{d^2} \left(\frac{1}{1+20(fd^2/UD)^{5.3}} \right)^{1/2} \tag{4.3}$$

where $F_{n1}\left[\frac{x}{D}\right]$ is the nonlinear relationship obtained from Figure 4.26. U denotes the mean velocity of the flow and f denotes the frequency. By using the values represented in Figure 4.26, a curve fitting is performed in order to represent $F_{n1}\left[\frac{x}{D}\right]$ as a function. The data points used to fit a curve for $F_{n1}\left[\frac{x}{D}\right]$ are represented in Table 4.3.

Table 4.3 An approximation of $F_{n1}[x/D]$ based on Figure 4.24 [22]

$\frac{x}{D}$	0	1	1.5	2	3	4	6	8	10	15	70
$F_{n1}\left[\frac{x}{D}\right]$	0	0.02	0.03	0.0355	0.025	0.01	0.004	0.003	0.0025	0.002	0.002

By using the values represented in Table 4.2, a curve fit is obtained by using curve fitting toolbox of MATLAB as,

$$F_{n1}[x] = \frac{0.07057x + 0.3849}{x^2 - 23.22x + 167.9}. \tag{4.4}$$

By substituting our flow variables in the Eq. (4.3), acoustic pressures are obtained (The MATLAB code is provided in Appendix D) showing the empirical results of Tobin and Chang [22]. Acoustic pressures and normalized acoustic pressures obtained by using empirical parameters are given in Figure 4.27 and 4.28, respectively.

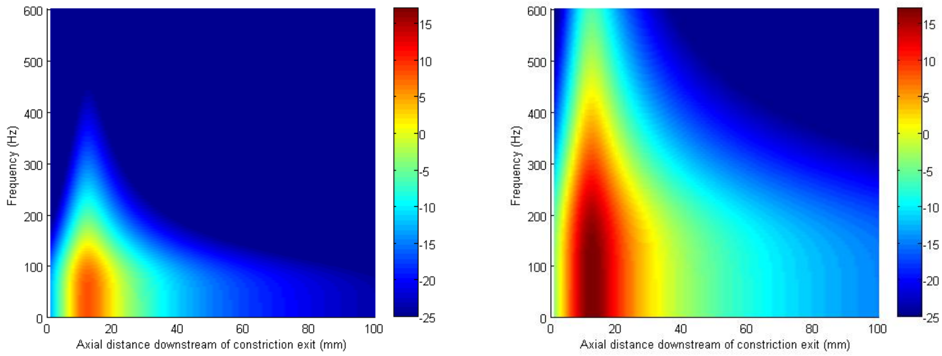

(a) (b)

Figure 4.27 Acoustic pressure (dB *re*: 1 Pa) near wall inner surface as function of axial position and frequency by using empirical parameters. All cases are for a tube with a constriction ending at 0 mm. (a) $Re_D = 1000$. (b) $Re_D = 2000$.

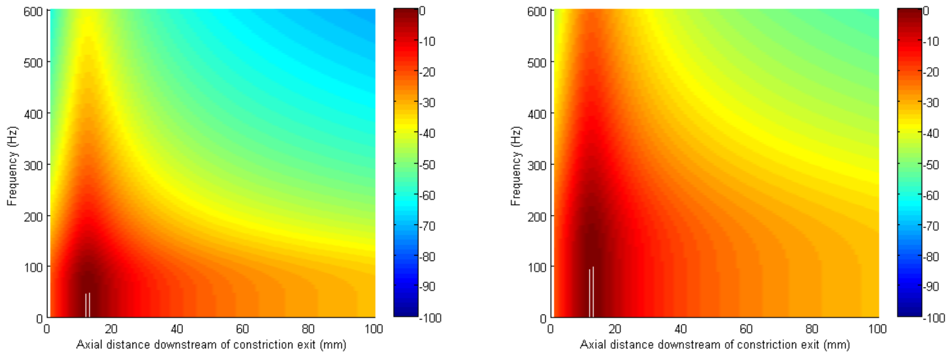

(a) (b)

Figure 4.28 Normalized acoustic pressure (dB *re*: Maximum spectral pressure) according to the highest pressure near wall inner surface as function of axial position and frequency by using empirical parameters. All cases are for a tube with a constriction ending at 0 mm. (a) $Re_D = 1000$. (b) $Re_D = 2000$.

Current numerical results, results obtained by the universal correlations provided by Tobin and Chang [22] and the experimental results provided by Yazicioglu et al. [21] are all in agreement in terms of general spectral behavior. The most active region is again the first 25 mm after the constriction exit and the amplitude of acoustic pressures decrease gradually as the frequency increases. However, once again the numerically found pressure amplitudes are much lower than the experimental findings. As can be seen from Figures 4.27 and 4.28, the point with highest fluctuating pressure amplitudes is approximately 15 mm downstream of constriction exit which is in agreement with the results of numerical simulations. In the numerical simulations, this corresponding point is found within 10-15 mm axial distance downstream of constriction exit.

4.3.2. Pressure and Axial Velocity Distributions of Flow for FSI Analyses

Pressure distributions obtained by FSI analyses are presented in Figure 4.29 and Figure 4.30 for $Re_D = 1000$ and 2000, respectively.

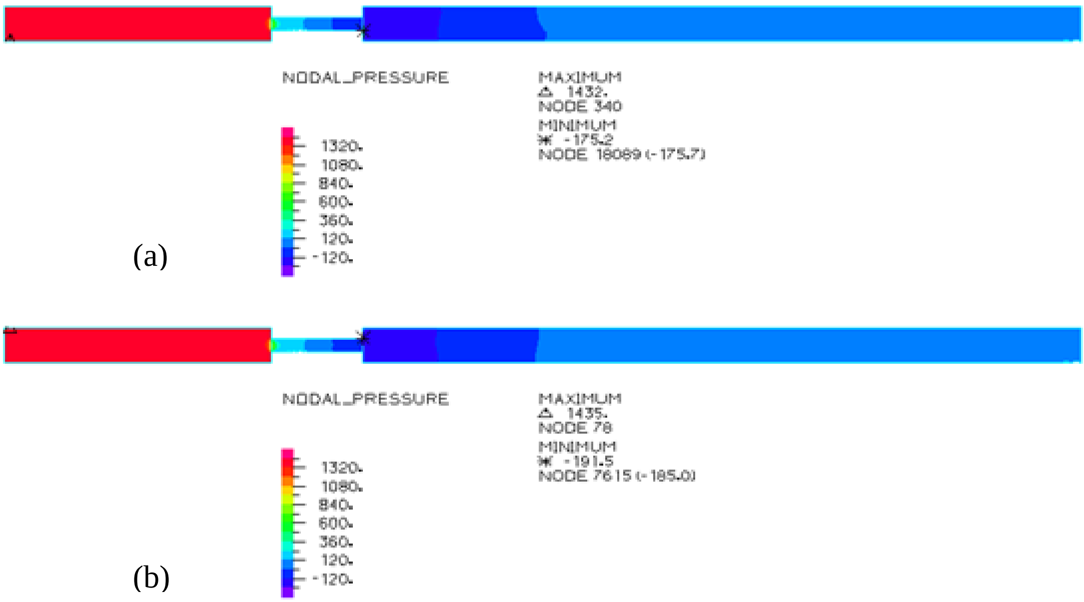

Figure 4.29 Instantaneous pressure (Pa) distribution of FSI analysis at $t = 1\ s$, by coupling flow mesh 2 and structure mesh 1. (a) DES, $Re_D = 1000$. (b) LES, $Re_D = 1000$.

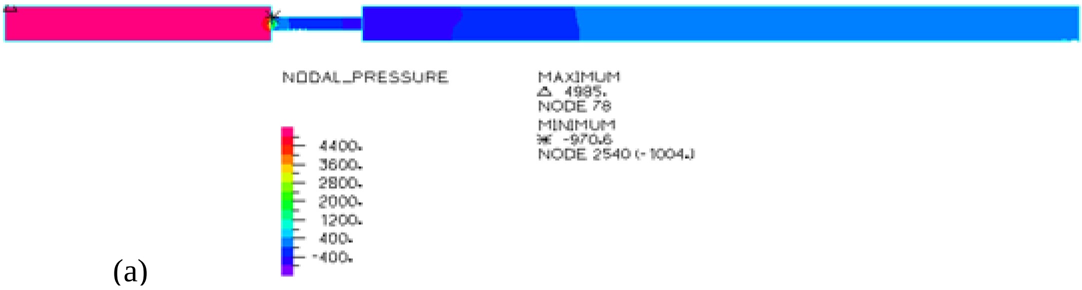

(a)

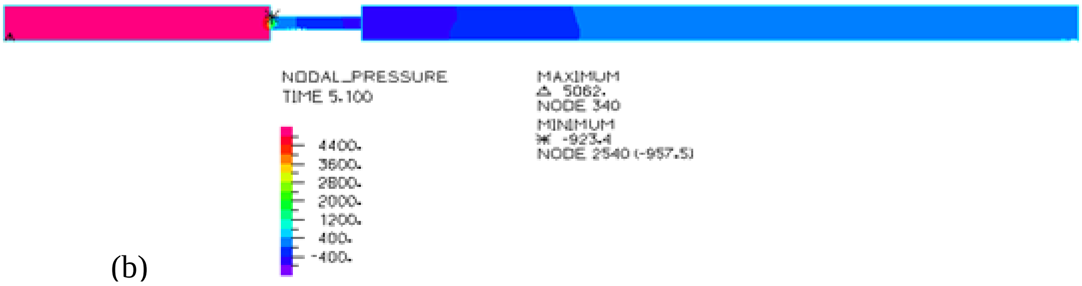

(b)

Figure 4.30 Instantaneous pressure (Pa) distribution of FSI analysis at $t = 1\ s$, by coupling flow mesh 2 and structure mesh 1. (a) DES, $Re_D = 2000$. (b) LES, $Re_D = 2000$.

Axial flow velocity distributions obtained by FSI analyses are presented in Figures 4.31 and 4.32 for $Re_D = 1000$ and 2000, respectively.

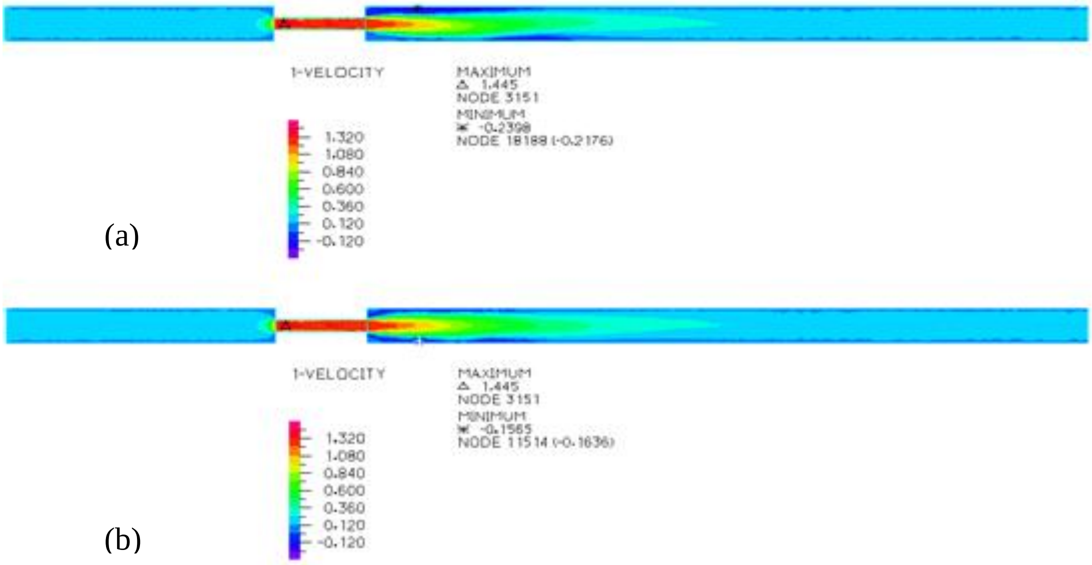

Figure 4.31 Instantaneous axial velocity (m/s) distribution obtained by FSI analyses at $t = 1\ s$, by coupling flow mesh 2 and structure mesh 1. (a) DES $Re_D = 1000$. (b) LES, $Re_D = 1000$.

(a)

(b)

Figure 4.32 Instantaneous axial velocity (m/s) distribution obtained by FSI analyses at $t = 1\ s$, by coupling flow mesh 2 and structure mesh 1. (a) DES $Re_D = 2000$. (b) LES, $Re_D = 2000$.

If the structure deforms significantly, then mean flow variables obtained by FSI analyses may change seriously when compared with the rigid wall assumption models. However, in our case, since the tubular structure does not deform considerably, the diameter of the flow domain remains nearly the same. Hence, mean flow velocities obtained by FSI analyses are similar to the results obtained by rigid wall assumption models. Mean wall pressures obtained by numerical simulations and experiments [21] for rigid and compliant tubes are presented in Figure 4.33.

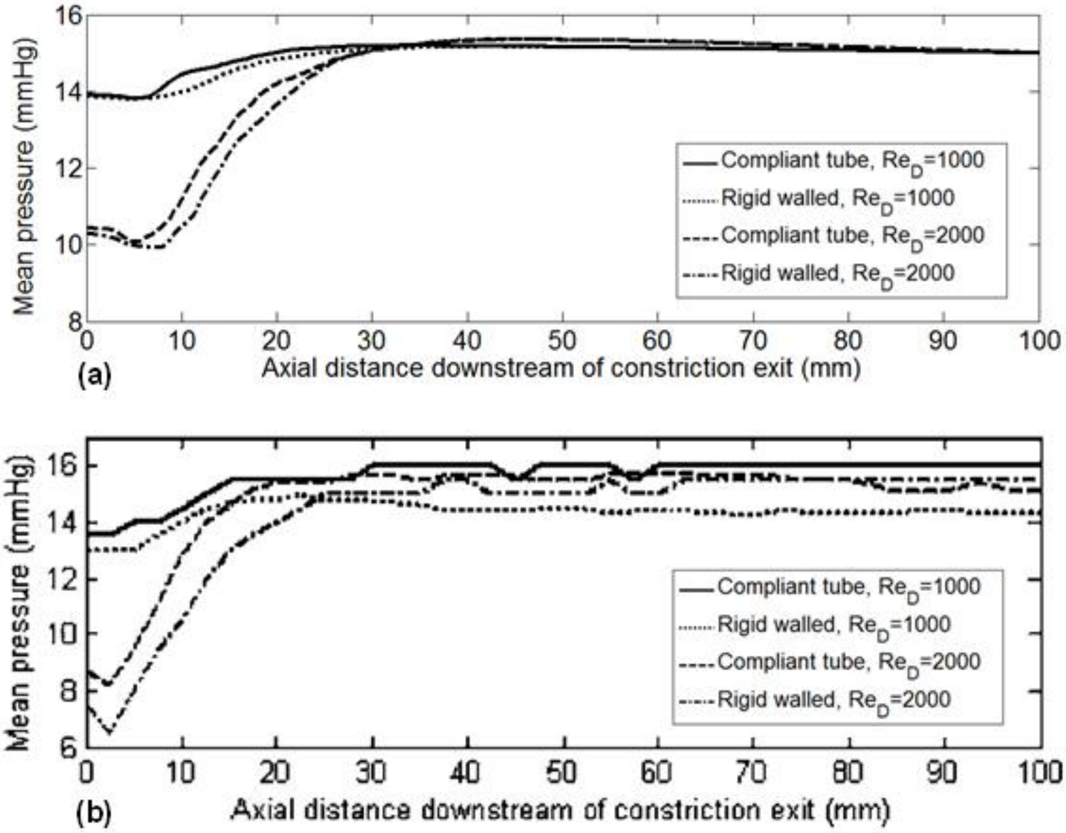

Figure 4.33 Mean wall pressures for rigid and compliant tube models. (a) Numerical results. (Rigid walled: DES, flow mesh 2; Compliant tube: FSI, flow mesh 2 + structure mesh 1). (b) Experimental [21] results.

Results presented in Figure 4.33 show good agreement with the experimental results where rigid walled tube models have slightly higher pressure drop when compared with compliant tube models.

4.3.3. Radial Velocities and Accelerations of Tube Wall for FSI Analyses

The nodes placed on the the tube wall will experience mainly radial deformation in the form of displacement, velocity and acceleration. The modal response and the natural frequencies of the fluid filled tube can be determined based on the radial velocity and accelaration of the nodes on the tubular structure.

The radial velocity of the nodes on the tube wall are extracted from the numerical simulations and hanning window is applied on the time domain data. In order to monitor the spectral behavior of the radial velocities on the compliant tube, FFT is performed on the windowed radial velocity data. (MATLAB code is available in Appendix E). The frequency distribution of radial velocities are given in Figures 4.34 and 4.35 for $Re_D = 1000$.

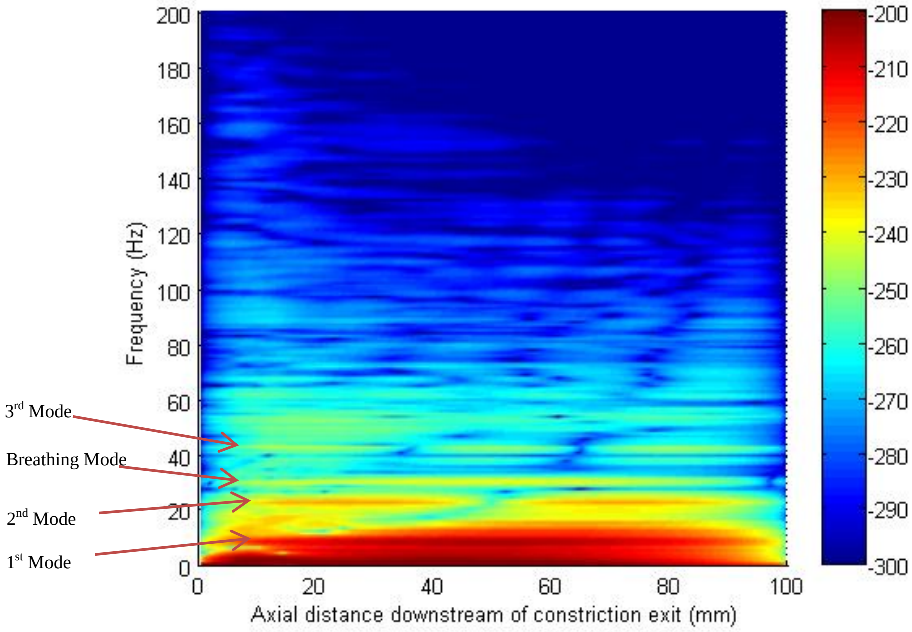

Figure 4.34 Compliant tube radial wall velocity (dB re: 1 m/s) as a function of axial position and frequency for DES, $Re_D = 1000$.

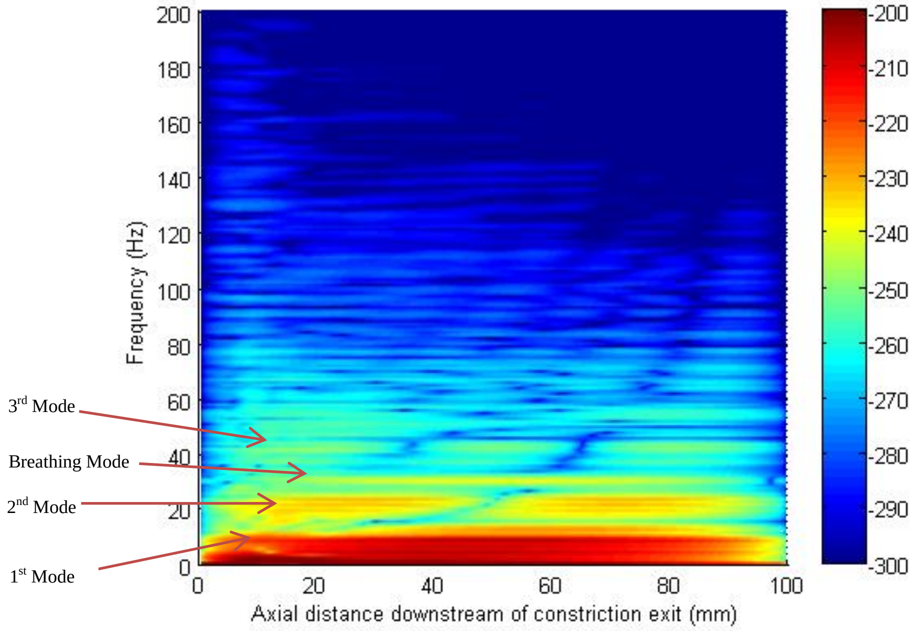

Figure 4.35 Compliant tube radial wall velocity (dB re: 1 m/s) as a function of axial position and frequency for LES, $Re_D = 1000$.

Using DES and LES models in FSI analyses, similar results are obtained. First 3 bending modes of the fluid filled tube are visible in Figure 4.34 and Figure 4.35. The frequency distribution of radial velocities are given in Figures 4.36 and 4.37 for $Re_D = 2000$.

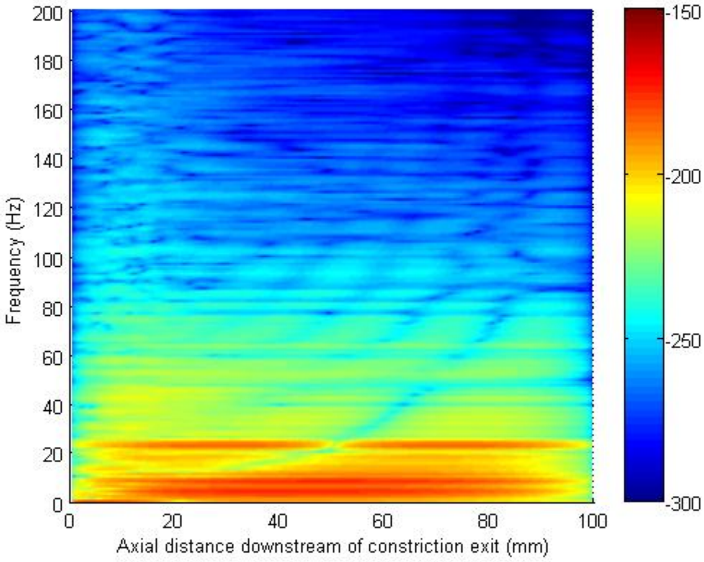

Figure 4.36 Compliant tube radial wall velocity (dB re: 1 m/s) as a function of axial position and frequency for DES, $Re_D = 2000$.

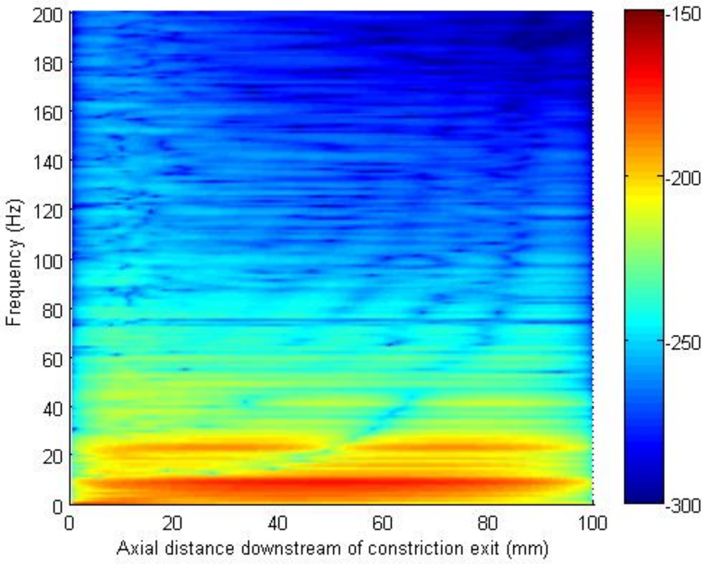

Figure 4.37 Compliant tube radial wall velocity (dB re: 1 m/s) as a function of axial position and frequency for LES, $Re_D = 2000$.

Similar modal response and natural frequencies are observed for $Re_D = 1000$ and 2000, in both numerical and experimental studies. For $Re_D = 2000$, a wider range of modes are apparent. For $Re_D = 1000$ case, we can clearly see the modes of the tube within 0-50 Hz. However, for $Re_D = 2000$, the modes are visible within 0-80 Hz since a wider range of frequencies are excited and the amplitudes of the acoustic pressures increase as the flow rate increases. Also, for the first 25 mm axial distance downstream of constriction exit, the spectral amplitudes of radial velocities are higher, since first 25 mm is the recirculation region and a more powerful excitation is present driving a wider band of frequencies. If we could excite the fluid filled tube for a wider range of frequencies, then we could see other modes of the tube. The frequency distribution of radial velocities obtained Yazicioglu et al. [21] are given in Figure 4.38.

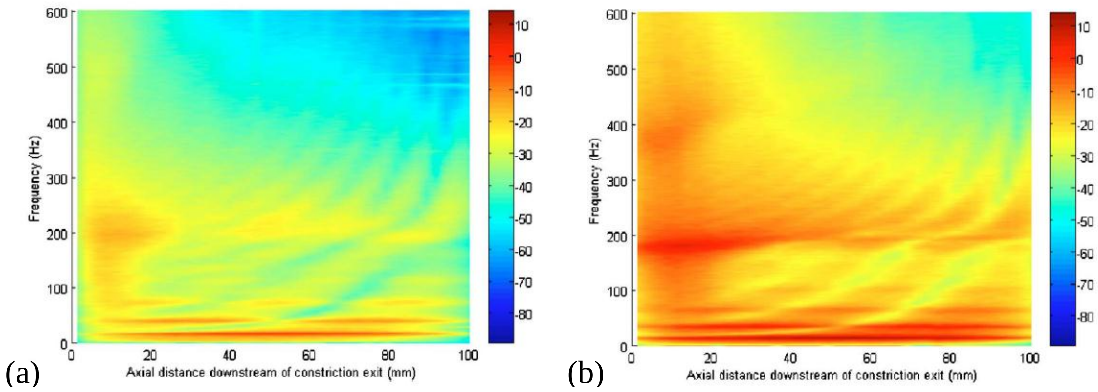

Figure 4.38 Constricted compliant tube radial wall velocity (dB re: 1 mm/s) as a function of axial position and frequency. (a) Experiment [21] in air, $Re_D = 1000$. (b) Experiment [21] in air, $Re_D = 2000$.

The results of the modal analysis, FSI analysis and exprerimental [21] results are compared in Table 4.4.

Table 4.4 Comparison of FSI analyses, modal analyses and experimental results

Mode	FSI Analyses	Modal Analyses	Experiments [21]
1^{st} Bending Mode	~ 9 Hz	9.04 Hz	~ 10 Hz
2^{nd} Bending Mode	~ 24 Hz	23.30 Hz	~ 30 Hz
1^{st} Breathing Mode	~ 30 Hz	30.61 Hz	Not Visible
3^{rd} Bending Mode	~ 42 Hz	42.45 Hz	~ 65 Hz

Mode shapes and natural frequencies obtained by FSI analyses and modal analysis support each other. However the frequencies obtained by experiments are higher than those predicted by the simulations. The discrepancy might be caused due to the simplistic linear elastic and isotropic modeling of the latex tube with the material properties retrieved from the general literature, which is a more complex hyperelastic and viscoelastic material in reality.

By using the radial velocities and accelations of a random node on the tube wall, the natural frequencies of the fluid filled structure can be obtained. FFT of the radial velocities and accelarations of a random node on the compliant tube wall is given in Figures 4.39 and 4.40 respectively.

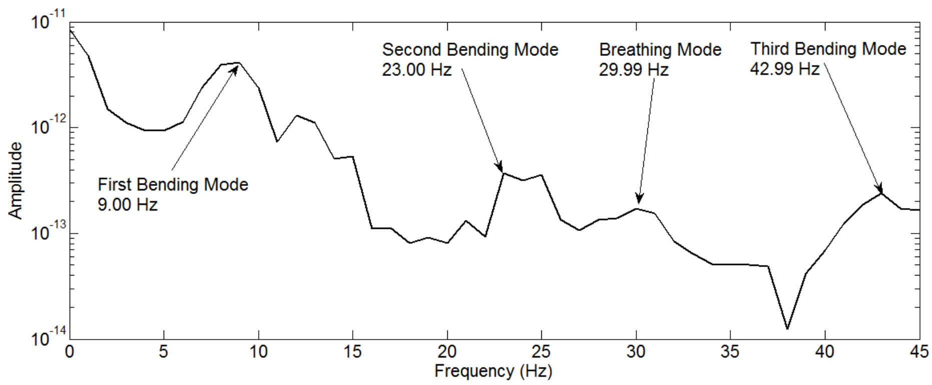

Figure 4.39 FFT of radial velocities of a random node on the compliant tube

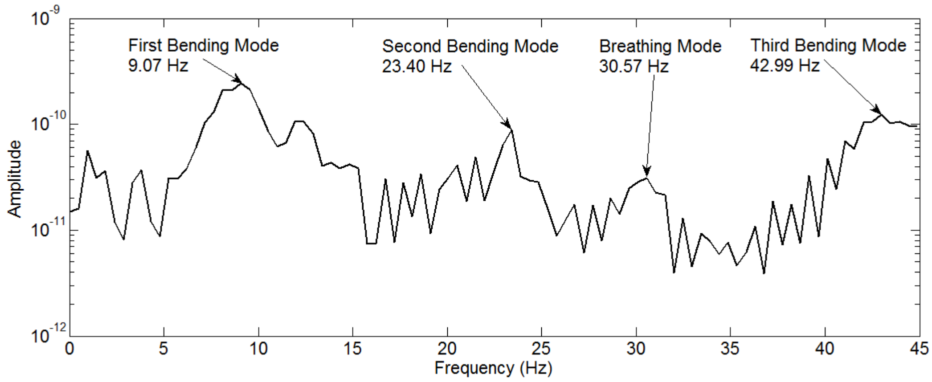

Figure 4.40 FFT of radial accelerations of a random node on the compliant tube

CHAPTER 5

CONCLUSION AND FUTURE WORK

5.1. Conclusion

Stenosed flows are investigated numerically by using commercial finite element software ADINA. Results of numerical simulations are compared with the results in literature. The simulations are performed by using rigid and compliant tube models. For the compliant tube model, the fluid model and structure model are coupled and solved by using ADINA-FSI. Dynamic acoustic pressures are obtained using the results of numerical simulations. The acoustic pressures obtained by numerical simulations showed a good agreement with the experimental results in literature in terms of general spectral behavior, but the amplitudes were significantly lower. Acoustic pressures obtained by numerical simulations showed that, at the exit of the constriction, there is a highly disturbed recirculation region exciting a wide range of frequencies. The length of the recirculation region is found approximately as $3.5D$ where D is the diameter of the tubular structure. The length of the recirculation region does not change significantly for $Re_D = 1000$ and 2000 cases. The axial distance where the maximum range of frequencies are excited, is nearly 15 mm downstream of the constriction exit. By using the radial wall velocities of the structure, the modal response of the fluid filled compliant tubular structure is obtained. The first three mode shapes and frequencies are clearly visible in the linear spectrum of the radial velocities of the tube. The results obtained by preforming modal analysis also led to similar results.

5.2. Future Work

This study can be taken as an initial step for modeling high frequency FSI problems encountered in cardiovascular system. Different levels of constricted flows can be modeled on various size vessels for a range of flow rates to create a knowledge base for the spectral signatures of these anomalies without the need for performing experiments for each combination.

As for future improvements, the flow geometry can be selected from a more realistic case obtained by medical imaging techniques. Non-Newtonian fluid behavior can be introduced for further improvement. The pulsatile nature of flow may be considered and solved for varying flow rates. Also a more appropriate material model can be used for the blood vessels. Surrounding tissue may also be included in the model to obtain the response on a simulated skin surface for the feasibility of non-invasive diagnostic techniques.

REFERENCES

[1] A. Maton, Human Biology and Health, 1993.

[2] W. Rosamond, K. Flegal, G. Friday, K. Furie, A. Go, K. Greenlund, N. Haase, M. Ho, V. Howard, B. Kissela, S. Kittner, D. Lloyd-Jones, M. McDermott, J. Meigs, C. Moy, G. Nichol, C. J. O'Donnell, V. Roger, J. Rumsfeld, P. Sorlie, J. Steinberger, T. Thom, S. Wasserthiel-Smoller and Y. Hong, "Heart Disease and Stroke Statistics - 2007 Update: A report from the American Heart Association Statistics Committee and Stroke Statistics Subcommittee," *Circulation*, vol. 115, no. 5, pp. e69-e171, 2007.

[3] V. Feigin, "Stroke Epidemiology in the Developing World," *Lancet,* vol. 365, no. 9478, pp. 2160-2161, 2005.

[4] N. Shammas, "Epidemiology, Classification, and Modifiable Risk Factors of Peripheral Arterial Disease," *Vascular Health and Risk Management,* vol. 3, no. 2, pp. 229-234, 2007.

[5] W. E. Zarins, "Compensatory Enlargement of Human Atherosclerotic Coronary Arteries," *New England Journal of Medicine,* vol. 316, no. 22, pp. 1371-1375, 1987.

[6] N. S. Sipahi, "Effect of Very High-Intensity Statin Therapy on Regression of Coronary Atherosclerosis: The ASTEROID Trial," *Journal of the American Medical Association,* vol. 295, no. 13, pp. 1556-1565, 2006.

[7] A. O. Borisyuk, “Experimental Study of Wall Pressure Fluctuations in a Pipe behind a Stenosis,” *International Journal of Fluid Mechanics Research,* vol. 30, no. 3, pp. 264-278, 2003.

[8] D. F. Young, “Fluid Mechanics of Arterial Stenoses.,” *Journal of Biomechanical Engineering,* vol. 101, no. 3, pp. 157-175, 1979.

[9] J. S. Stroud, S. A. Berger and D. Saloner, “Numerical Analysis of Flow Through a Severely Stenotic Carotid Artery Bifurcation,” *Journal of Biomechanical Engineering,* vol. 124, no. 1, pp. 9-20, 2002.

[10] P. Doriot, P. Dorsaz, L. Dorsaz and W. Rutishauser, “Overestimation of Stenosis Severity by Single Plane Geometric Measurements,” *Computers in Cardiology,* vol. 0, no. 0, pp. 109-112, 1996.

[11] R. S. Lees and C. F. Dewey, “Phonoangiography: A New Noninvasive Diagnostic Method for Studying Arterial Disease.,” *Proceedings of the National Academy of Sciences of the United States of America,* vol. 67, no. 2, pp. 935-942, 1970.

[12] J. J. Fredberg, “Pseudo-Sound Generation at Atherosclerotic Constrictions in Arteries.,” *Mass Inst Technol, Fluid Mech Lab, Publ,* no. 72-9, 1972.

[13] J. J. Fredberg, “Origin and Character of Vascular Murmurs: Model Studies,” *Journal of the Acoustical Society of America,* vol. 61, no. 4, pp. 1077-1085, 1977.

[14] G. W. Duncan, J. O. Gruber and C. F. Dewey, "Evaluation of Carotid Stenosis by Phonoangiography," *New England Journal of Medicine,* vol. 293, no. 22, pp. 1124-1128, 1975.

[15] W. H. Pitts and C. F. Dewey, "Spectral and Temporal Characteristics of Post-Stenotic Turbulent Wall Pressure Fluctuations.," *Journal of Biomechanical Engineering,* vol. 101, no. 2, pp. 89-95, 1979.

[16] A. O. Borisyuk, "Model Study of Noise Field in the Human Chest due to Turbulent Flow in a Larger Blood Vessel," *Journal of Fluids and Structures,* vol. 17, no. 8, pp. 1095-1110, 2003.

[17] A. O. Borisyuk, "Modeling of Noise Generation by a Vascular Stenosis," *International Journal of Fluid Mechanics Research,* vol. 29, no. 1, pp. 65-86, 2002.

[18] L. D. Jou and D. Saloner, "A Numerical Study of Magnetic Resonance Images of Pulsatile Flow in a Two Dimensional Carotid Bifurcation a Numerical Study of MR Images," *Medical Engineering and Physics,* vol. 20, no. 9, pp. 643-652, 1998.

[19] M. T. Pittard, "Large Eddy Simulation Based Turbulent Flow-Induced Vibration of Fully Developed Pipe Flow," M.Sc. Thesis in Brigham Young University, 2003.

[20] R. A. Cassanova and D. P. Giddens, "Disorder Distal to Modeled Stenoses in Steady and Pulsatile Flow," *Journal of Biomechanics,* vol. 11, no. 10-12, pp.

441-453, 1978.

[21] Y. Yazicioglu, T. J. Royston, T. Spohnholtz, B. Martin, F. Loth and H. S. Bassiouny, "Acoustic Radiation from a Fluid-Filled, Subsurface Vascular Tube with Internal Turbulent Flow due to a Constriction," *Journal of the Acoustical Society of America,* vol. 118, no. 2, pp. 1193-1209, 2005.

[22] R. J. Tobin and I. D. Chang, "Wall Pressure Spectra Scaling Downstream of Stenoses in Steady Tube Flow," *Journal of Biomechanics,* vol. 9, no. 10, pp. 633-640, 1976.

[23] S. E. Lee, S. Lee, P. F. Fischer, H. S. Bassiouny and F. Loth, "Direct Numerical Simulation of Transitional Flow in a Stenosed Carotid Bifurcation," *Journal of Biomechanics,* vol. 41, no. 11, pp. 2551-2561, 2008.

[24] K. Khanafer and R. Berguer, "Fluid-structure Interaction Analysis of Turbulent Pulsatile Flow within a Layered Aortic Wall as Related to Aortic Dissection," *Journal of Biomechanics,* vol. 42, no. 16, pp. 2642-2648, 2009.

[25] D. Tang, C. Yang, Y. Huang and D. N. Ku, "Wall Stress and Strain Analysis Using a Three-Dimensional Thick-Wall Model with Fluid-Structure Interactions for Blood Flow in Carotid Arteries with Stenoses," *Computers and Structures,* vol. 72, no. 1, pp. 341-356, 1999.

[26] A. Valencia and M. Villanueva, "Unsteady Flow and Mass Transfer in Models of Stenotic Arteries Considering Fluid-Structure Interaction," *International Communications in Heat and Mass Transfer,* vol. 33, no. 8, pp. 966-975, 2006.

[27] D. Tang, J. Yang, C. Yang and D. N. Ku, “A Nonlinear Axisymmetric Model with Fluid-Wall Interactions for Steady Viscous Flow in Stenotic Elastic Tubes,” *Journal of Biomechanical Engineering,* vol. 121, no. 5, pp. 494-501, 1999.

[28] T. Shurtz, “Analysis of Induced Vibrations in Fully-Developed Turbulent Pipe Flow using a Coupled LES and FEA Approach,” M.Sc. Thesis in Brigham Young University, 2009.

[29] A. Bajoria, “Computational Wind Engineering using Finite Element Package ADINA,” M.Eng. Thesis in Massachusetts Institute of Technology, 2008.

[30] R. Darby, Chemical Engineering Fluid Mechanics, 2001.

[31] P. R. Spalart, “Strategies for Turbulence Modelling and Simulations,” *International Journal of Heat and Fluid Flow,* vol. 21, no. 3, pp. 252-263, 2000.

[32] P. Spalart, W. Jou, M. Strelets and S. Allmaras, “Comments of Feasibility of LES for Wings, and on a Hybrid {RANS/LES} Approach,” 1997.

[33] P. R. Spalart and S. R. Allmaras, “One-Equation Turbulence Model for Aerodynamic Flows,” *Recherche Aerospatiale,* no. 1, pp. 5-21, 1994.

[34] A. Travin, M. Shur, M. Strelets and P. Spalart, “Detached-Eddy Simulations Past a Circular Cylinder,” *Flow, Turbulence and Combustion,* vol. 63, pp. 293-313, 2000.

[35] S. Pope, Turbulent Flows, 2000.

[36] V. Krishnan, "Advancing Detached-Eddy Simulation," Ph.D. Thesis in Arizona State University, 2008.

[37] M. Germano, U. Piomelli, P. Moin and W. H. Cabot, "A Dynamic Subgrid-Scale Eddy Viscosity Model," *Physics of Fluids A,* vol. 3, no. 7, pp. 1760-1765, 1991.

[38] S. A. Berger and L. Jou, Flows in Stenotic Vessels, vol. 32, 2000, pp. 347-382.

[39] F. Iudicello, M. W. Collins, F. S. Henry, J. C. Jarvis, A. Shortland, R. Black and S. Salmons, *Review of Modelling for Arterial Vessels - Simplified Ventricular Geometries,* vol. 9, 1996, pp. 179-194.

[40] W. Jin-Zhao, T. Bing, W. Welkowitz, J. L. Semmlow and J. B. Kostis, "Modeling Sound Generation in Stenosed Coronary Arteries," *IEEE Transactions on Biomedical Engineering,* vol. 37, no. 11, pp. 1087-1094, 1990.

[41] C. Clark, "Turbulent Wall Pressure Measurements in a Model of Aortic Stenosis," *Journal of Biomechanics,* vol. 10, no. 8, pp. 461-472, 1977.

[42] B. M. Kim and W. H. Corcoran, "Experimental Measurements of Turbulence Spectra Distal to Stenoses," *Journal of Biomechanics,* vol. 7, no. 4, pp. 335-342, 1974.

[43] S. Lee, P. F. Fischer, F. Loth, T. J. Royston, J. K. Grogan and H. S. Bassiouny, "Flow-induced vein-wall vibration in an arteriovenous graft," *Journal of Fluids and Structures*, vol. 20, no. 6 SPEC. ISS., pp. 837-852, 2005.

[44] "ADINA Theory and Modeling Guide Volume III: ADINA CFD & FSI (October 2005)".

APPENDIX A

MODELING IN ADINA

In this section, the modeling procedure by using ADINA will be explained. First the CFD model of the fluid flow will be explained and simulations with rigid wall assumption will be conducted by using this model. After that fluid filled structure model will be explained and modal analysis will be conducted by using the structure model. Finally, the fluid model and structure model will be coupled and FSI analysis will be conducted by coupling these models.

A.1. Fluid Flow Modeling in ADINA-CFD

ADINA-CFD is a module of ADINA AUI (ADINA User Interface) which is used to model the fluid flow. The processes will be described in such a way that the reader of this thesis can follow the same procedure easily.

A.1.1. Defining Problem Geometry

By using ADINA-M, which is the module used to model geometries, the flow domain can be formed. It is also possible to import data from other CAD (Computer-Aided Design) software by using parasolid data format. In our case, the geometry is constructed in a CAD software and saved using parasolid format and then imported to ADINA **(ADINA CFD → ADINA-M → Import Parasolid Model)**.

In our flow model, a domain which consists of seven bodies is created as shown in Figure A.1. The reason for these different bodies is the need for having different mesh densities in the flow domain. It is required that the mesh density should be high around the constriction region and downstream of the constriction exit.

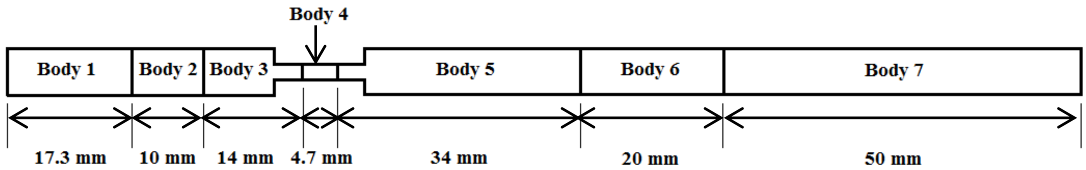

Figure A.1 Cross sectional view of flow domain consisted by 7 bodies

After creating the bodies, the face links between the bodies should be defined. This is an important point because if the mutual faces at neighbor bodies are not defined, these faces will act as rigid walls. By defining all the face links between the bodies, the bodies will behave as a united body **(ADINA CFD → Geometry → Faces → Face Link)**.

A.1.2. Flow Assumptions for the Fluid Model

The problem is solved in spatial domain in three dimensions. The fluid is modeled as an incompressible fluid and the heat transfer aspect of the problem is insignificant. Two different approaches are used for flow model which are DES and LES.

A.1.3. Detached Eddy Simulation

A.1.3.1. Boundary and Initial Conditions

In ADINA-CFD, there are four options for the flow model. These are laminar, turbulent *k-ε*, turbulent *k-ω/SST* and turbulent Spalart-Allmaras flow models. Since the DES option is only available in the turbulent Spalart-Allmaras model, it is selected to be able to perform DES **(ADINA CFD → Model → Flow Assumptions)**.

The fluid properties are defined from ‘Manage material properties’ section. There are many parameters used in the DES method as mentioned in previous chapter. All the DES parameters are used in ADINA CFD as default, as the same values used in literature [34]. Since DES parameters are empirical constants, for different flow cases, it is possible to change values of those parameters when necessary. Only fluid viscosity and density parameters are entered as seen in Figure A.2.

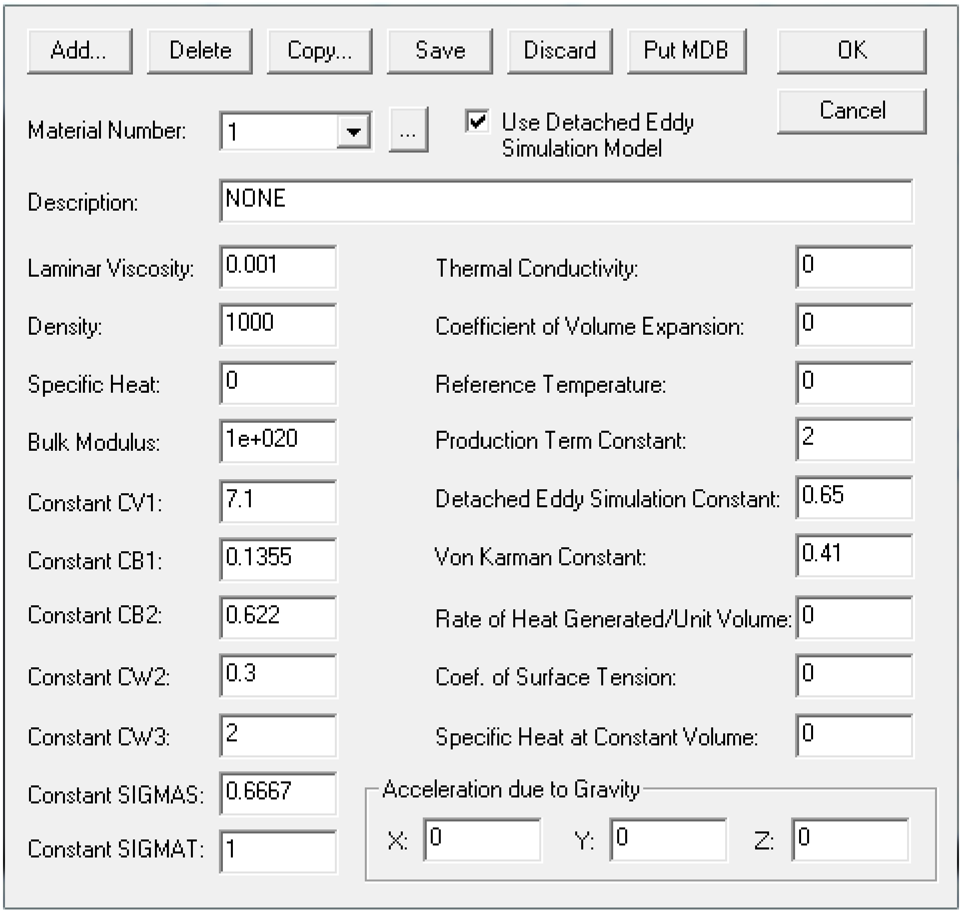

Figure A.2 DES parameters

(ADINA CFD → Model → Materials → Manage Materials → Spalart-Allmaras Model)

A prescribed uniform velocity profile is introduced at the inlet of the fluid domain **(ADINA CFD → Model → Usual Boundary Conditions/Loads → Apply → Velocity → Define)**. The boundary conditions are adjusted for wall boundary conditions and no slip boundary condition is used at the wall boundaries as shown in Figure A.3.

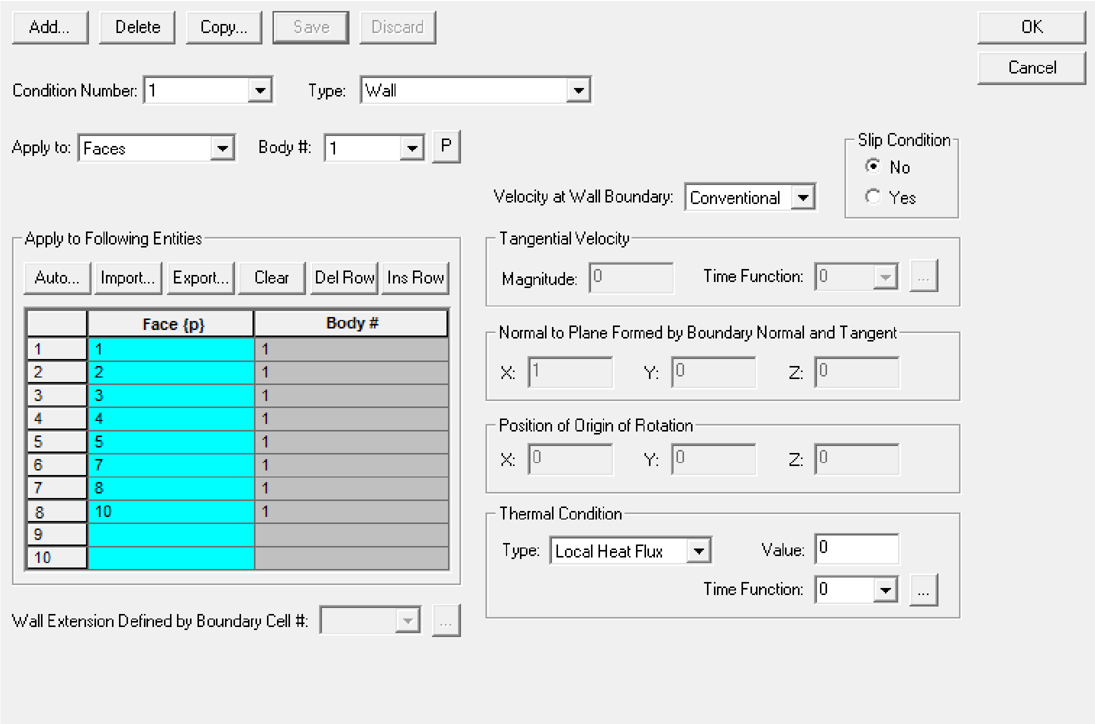

Figure A.3 Defining wall boundary conditions with no-slip condition

(ADINA CFD → Model → Special Boundary Condition)

Before meshing the geometry, the initial conditions and turbulence load at the inlet should be defined. If the initial conditions or turbulence load at the inlet is not defined in an appropriate way, ADINA-F will issue a warning when starting to solve the problem. ADINA-F is the solver for models defined by using ADINA CFD. ADINA-F solver recommends appropriate values for the solution.

Initial conditions for kinetic energy, K and rate of energy dissipation, E are applied to whole flow geometry by using Eq. (A.1) and Eq. (A.2) **(ADINA CFD → Model → Initial Conditions → Define)**.

A prescribed value for kinetic energy is defined at the inlet of the flow domain by using Eq. (A.1) **(ADINA CFD → Model → Usual Boundary Conditions/Loads → Apply → Turbulence → Define)**.

$$K = 1.5(iV)^2, \tag{A.1}$$

$$E = \frac{K^{1.5}}{0.3L} \tag{A.2}$$

where $V,\ L,\ i$ are velocity scale, length scale and turbulence intensity, respectively. For the velocity and length scale, inlet velocity $(0.15625\, m/s\ for\ Re_D = 1000, 0.3125\, m/s\ for\ Re_D = 2000)$ and the diameter of the tube $(6.4\, mm)$ is used respectively. The recommended turbulence intensity value by ADINA should be within 0.01 ~ 0.1. For our simulations turbulence intensity value is assigned to 0.025 as default for turbulence models. Also in similar simulations performed in literature by using ADINA, turbulence intensity value of 0.025 is used [29]. Prescribed inlet velocity, turbulence load introduced at the inlet and boundary conditions applied in flow model are shown in Figure A.4. The graphic window should look like Figure A.4 after completing the flow model.

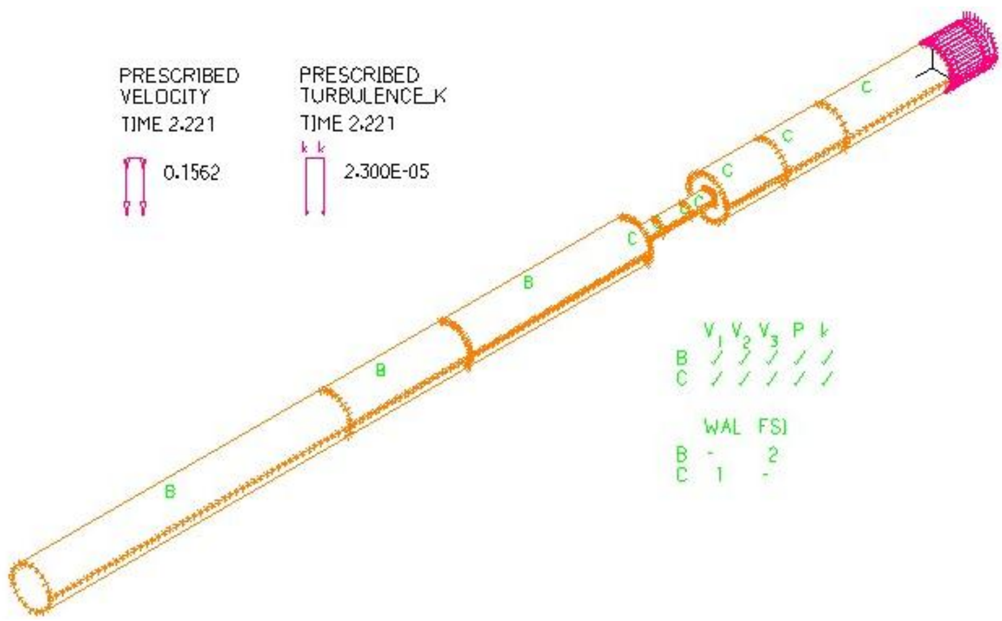

Figure A.4 Final view of completed flow model

A.1.3.2. Time Function, Time Step and Solution Process

The time function is related with the inlet velocity and turbulence load in the model. The prescribed inlet velocity profile and turbulence load are applied according to the time function defined as shown in Figure A.5.

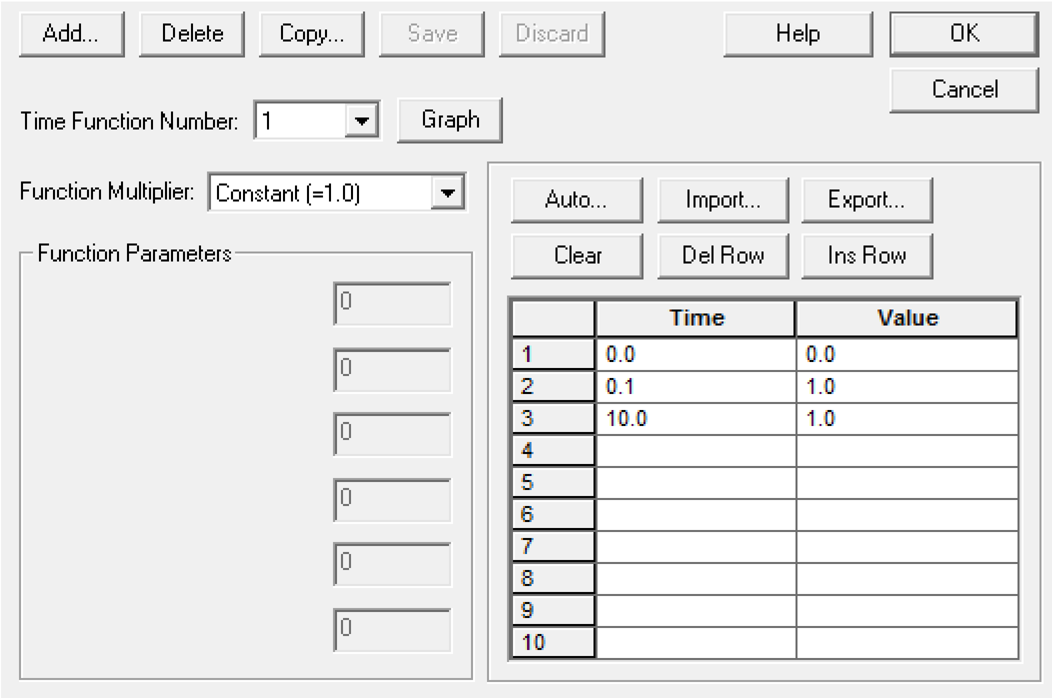

Figure A.5 Time function for flow model

(ADINA CFD → Control → Time Function)

As can be seen from the time function, the inlet velocity is equal to zero at the beginning of the analysis. Then within a time period of 0.1 s, inlet velocity reaches the assigned value and remains constant till the end of simulation. For transient analysis, the number and magnitude of the time steps should be defined **(ADINA CFD → Control → Time Step)**. Since the interest of this investigation is the turbulent induced wall vibrations, small time increments should be used in order to capture the behavior for a wider range of frequencies. First, the flow is solved for 100 time steps of 0.01 second. The flow variables reach to quasi-steady values after 100 time steps. Then 4500 time steps of 0.00024414 (1/4096) second are solved and the nodal pressures at the nodes on the wall are recorded. The recorded data is used to monitor the spectral behavior of the fluctuating variables of flow.

FCBI-C (Flow Condition Based Interpolation) type of element formulation is used in the simulations **(ADINA CFD → Control → Solution Process)**. FCBI-C type elements enable to solve large problems by using less memory when compared with other element formulations. In this element type all degrees of freedoms are defined at the center of the element and variables are assumed as piecewise constant in element during the computation and the final solution is interpolated at the corner nodes for post-processing [44]. It is indicated that FCBI-C elements are appropriate for incompressible, slightly compressible and low-speed compressible flows [44]. When FCBI-C element formulation is used, ADINA use AMG (Algebraic Multigrid) method as equation solver by default. Otherwise the equation solver is automatically selected as sparse solver.

For time integration, Euler backwards is used as default by ADINA. There is a parameter called 'Integration Parameter', which can be selected within the range of 0.5 – 1.0. If the integration parameter is selected as 0.5, this corresponds to the trapezoidal rule. By default the integration parameter is set to 1.0 in ADINA and this value corresponds to Euler backwards integration. In the simulations, Euler backward integration method is used **(ADINA CFD → Analysis Options)**.

A.1.4. Mesh Details for CFD Model

The geometry should be discretized into finite elements after defining the inlet velocity, boundary and initial conditions of the flow. In order to discretize the flow domain, first the element group should be defined in ADINA-CFD. Since the flow geometry is three-dimensional, 3-D fluid element group is defined **(ADINA CFD → Meshing → Element Groups → Advanced)**.

The geometries are discretized with different ratios and the bodies closer to the constriction area have more mesh density. Bodies are discretized by using element edge length parameter. As the element edge length gets smaller, a body will have higher mesh density **(ADINA CFD → Meshing → Mesh Density → Body)**. In order to check the mesh independency of the numerical solution, the simulations are performed by using three mesh types with different mesh sizes. The details of flow mesh 1, flow mesh 2, flow mesh 3 are given in Tables A.1, A.2, A.3 respectively.

Table A.1 Details of flow mesh 1

Body Number	Element Edge Length	Nodes on Axial Flow Direction	Nodes on Radial Direction
1	1.1 mm	17	7
2	0.8 mm	14	9
3	0.6 mm	25	12
4	0.55 mm	10	6
5	0.55 mm	63	13
6	0.85 mm	25	9
7	1.2 mm	43	7

Table A.2 Details of flow mesh 2

Body Number	Element Edge Length	Nodes on Axial Flow Direction	Nodes on Radial Direction
1	1 mm	19	8
2	0.75 mm	15	10
3	0.5 mm	29	14
4	0.4 mm	13	17
5	0.4 mm	86	17
6	0.7 mm	30	11
7	1 mm	51	8

Table A.3 Details of flow mesh 3

Body Number	Element Edge Length	Nodes on Axial Flow Direction	Nodes on Radial Direction
1	1 mm	19	8
2	0.675 mm	16	11
3	0.38 mm	38	18
4	0.32 mm	16	21
5	0.32 mm	108	21
6	0.5 mm	41	14
7	0.75 mm	68	10

The 3-D fluid elements are created according to the element edge lengths already defined. Delaunay meshing algorithm is used for the unstructured mesh and 4-node tetrahedral elements are created **(ADINA CFD → Meshing → Create Mesh → Body)**.

The 3D tetrahedral element (4-node) is shown in the Figure A.6. For 3D tetrahedral element, all variables are defined at the corner nodes. There is a central node which is an 'auxiliary' node where only the velocity is defined [44]. This element can be used for flows with high and low Reynolds numbers.

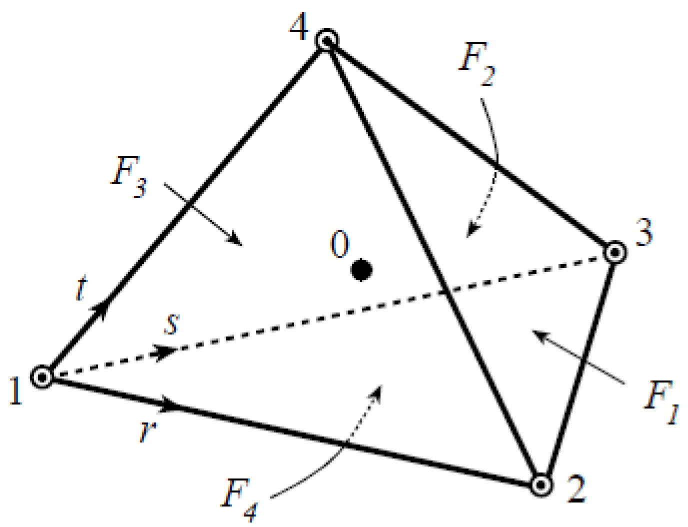

Figure A.6 Tetrahedral element [44]

The comparison of the total element numbers of the created meshes is shown in Table A.4.

Table A.4 Comparison of total number of elements

Mesh #	Number of Elements
Fluid mesh 1	82215
Fluid mesh 2	145872
Fluid mesh 3	304927

For all three mesh types, regions close to the constriction, the mesh density becomes higher and as the distance from the constricted area increase, the mesh density gets decreased. Sectional views of the constricted area for the different types of meshes are shown in Figures A.7, A.8 and A.9.

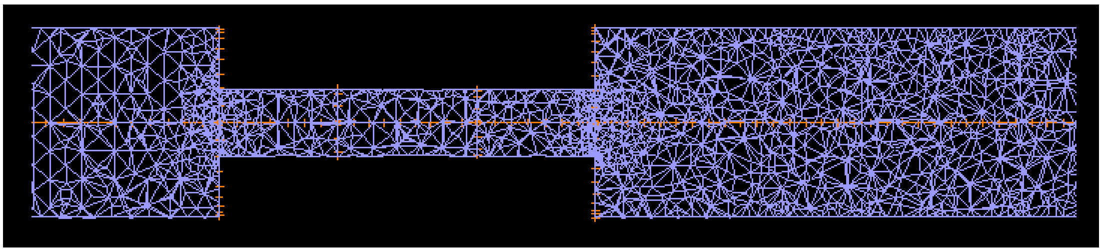

Figure A.7 Cross section of the flow mesh 1

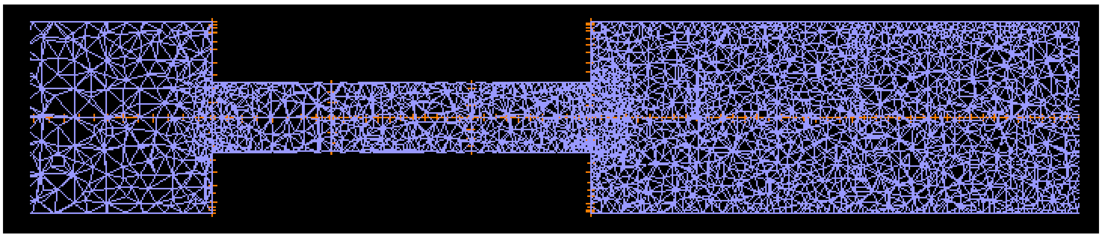

Figure A.8 Cross section of the flow mesh 2

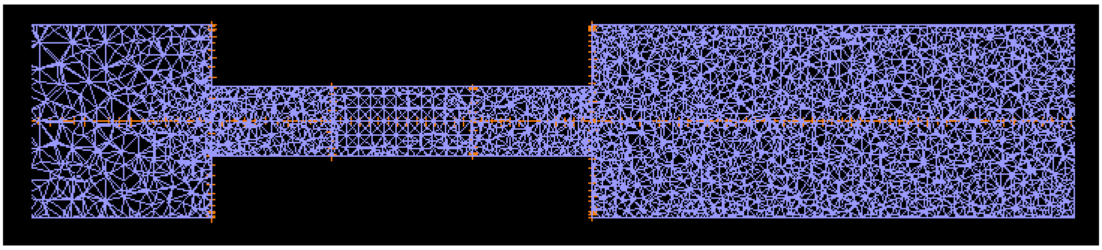

Figure A.9 Cross section of the flow mesh 3

A.1.5. Large Eddy Simulation

The procedure performed for DES model is nearly the same with the LES model. In ADINA-CFD, LES model becomes available when the flow model is selected as laminar **(ADINA CFD → Model → Flow Assumptions)**.

There are several parameters used for LES. Since the heat transfer in the fluid domain is not important, the thermal conductivity and rate of heat generated are set to zero. Viscosity and density of the fluid are again the same as the values used in the DES model. Model parameters for LES are shown in Figure A.10.

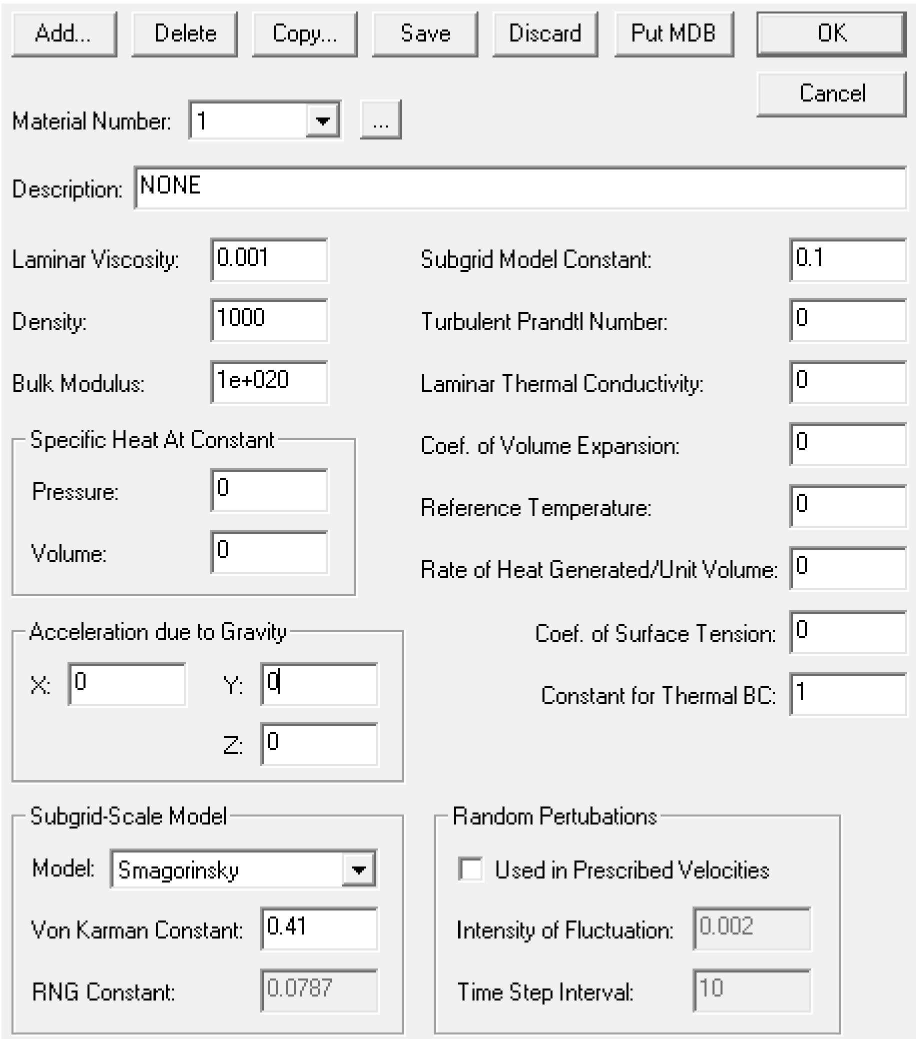

Figure A.10 Model parameters for LES

(ADINA CFD → Model → Materials → Manage Materials → Large Eddy Simulation Model)

For Subgrid-Scale model, there are three options in ADINA-CFD which are standard, Smagorinsky and renormalization group. In this study Smagorinsky model is used for the subgrid-scaling. Smagorinsky model constant should be within 0.1 – 0.25. In literature there are some simulations performed by using Smagorinsky constant as 0.1 [19, 28]. It is also stated that the Smagorinsky constant does not affect the solution seriously [19, 28]. In the simulations performed, the Smagorinsky constant is used as 0.1. Von Karman constant is set to 0.41 by default in ADINA as used in the literature.

Initial turbulent kinetic energy and initial energy dissipation rate values are applied for DES, because if the appropriate initial conditions are not applied for fluid domain ADINA-F issues a warning. In contrary, initial turbulent kinetic energy and energy dissipation rate values are not defined for LES and ADINA-F does not issue any warning about initial conditions. The time steps, time functions, meshing algorithms, mesh sizes used and other parameters are the same for DES and LES models.

A.2. Structure Model

In order to model the structure, ADINA Structures module is used. In the current problem, the last 100 mm of the flow interacts with the structure (See Figure 3.5). Therefore, a tube with 100 mm length is modeled as elastic and isotropic. As the material of the tube, latex rubber material properties are used in order to mimic the experimental conditions in the literature [21, 22]. Latex rubber material properties and geometrical dimensions of the tube structure are shown in Table A.5. As in the fluid model, heat transfer is neglected for the structure model.

Table A.5 Material properties and geometric dimensions of structure

Parameter	**Value**
Inner diameter of flexible tube	6.4 mm
Length of flexible tube	100 mm
Wall thickness of flexible tube	0.3 mm
Density of latex tube material	1086 kg/m^3
Young's modulus for latex tube material	800 kPa
Poisson's ratio for latex tube material	0.495

A.2.1. Modal Analysis of the Structure

Structure model is used for two different analysis which are modal analysis of the structure and FSI analysis. In order to find the modes and natural frequencies of the fluid filled structure, 'Frequencies/Modes' section should be selected in ADINA Structures. If this section is chosen as 'Dynamics-Implicit' as it will be described in the following sections, then the structure model can be used for coupled solution of FSI analysis.

A.2.1.1. Defining Materials for Structure Model

3-D solid and 3-D fluid materials are defined for structure and internal fluid, respectively. Default parameters which are set by ADINA are used for solid and fluid material definition. Kinematic formulations are also used as default **(ADINA Structures → Meshing → Element Groups)**.

A.2.1.2. Defining Properties of Materials

In all of our simulations by using ADINA models, parameters are used according to SI units. Properties of fluid model are used as the water properties **(ADINA Structures → Model → Materials → Manage Materials → Potential-based Fluid)**. Properties of tubular vessel are used as the latex rubber properties **(ADINA Structures → Model → Materials → Manage Materials → Isotropic)**.

A.2.1.3. Solution Methods for Modal Analysis

There are 3 different methods in ADINA Structure as solution methods which are determinant-search, subspace iteration and Lanczos iteration methods. For determining the modes of the structure, the fluid domain inside the structure should also be taken into account. Since there is a fluid medium inside the structure, ADINA gives an alert at the beginning of the solution. It is noted that if the fluid potential degree of freedom is active, then Lanczos iteration method is recommended. Therefore, Lancroz iteration method is used for determining the frequencies and mode shapes of the structure with internal fluid **(ADINA Structures → Analysis Options)**.

A.2.1.4. Boundary Conditions, Loads and Degrees of Freedom for Structure

For both modal analysis and FSI analysis, the structure ends are modeled as fixed supports **(ADINA Structures → Model → Boundary Conditions → Apply Fixity)**. Hence, translational and rotational motion at both ends are set to zero. The master degrees of freedom are set as translations along the X, Y and Z axes **(ADINA Structures → Control → Degrees of Freedom)**. ADINA uses 'Sparse' solver as default for structures, which is used for modal analysis of structure. There are also multigrid, iterative and direct solver options other than the sparse solver.

The mean dynamic pressure inside the latex tube is measured as 15 mmHg in the experiment performed by Yazicioglu et al. [21]. In order to incorporate the fluid pressure inside the vessel structure, 15 mmHg (2000 Pa) pressure load is applied at the inner surface of the structure.

A.2.1.5. Mesh Details for Structure

8-node solid and fluid elements are created for modal analysis (**ADINA Structures → Meshing → Create Mesh → Volume)**. Totally, 96000 elements are created for the structure model which is composed of 16000 solid elements and 80000 potential based fluid elements. The structure model which is composed of solid and fluid elements is coupled with the previously described flow model to perform FSI analysis. If a structure model which only contain solid elements for tube is coupled with previously defined flow model in FSI analysis, then the modes of an empty tube is obtained. If the structure model includes both solid and fluid elements for tube and fluid inside the tube, then the modes of a fluid filled tube is obtained. Created fluid mesh in the structure model is independent from previously created flow model. Since the vibrational modes of fluid-filled tube is in interest, a stagnant fluid domain is defined inside the tube.

Solid mesh has 3, 41 and 201 uniform nodes in radial, circumferential and axial directions, respectively. Corresponding numbers for the fluid mesh are 11, 41 and 201. The structure mesh composed of fluid and solid elements is shown in Figure A.11.

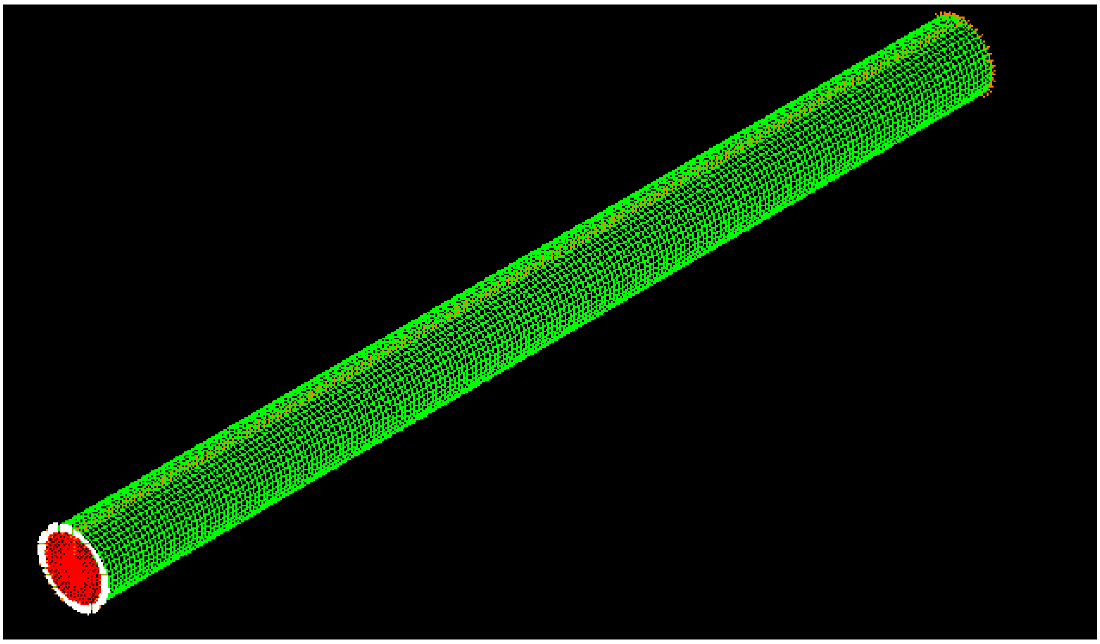

Figure A.11 Mesh generated for structure model

A.3. FSI in ADINA

The flow and structural models are solved together in order to get structural vibrations due to the fluid flow. Since the fluid model and structure model has to be coupled, there needs to be some modifications in fluid and structure models. Note that a fluid-filled tube is coupled with a turbulent fluid flow in the FSI analysis.

For the fluid model, the option of FSI should be selected. After activating FSI mode, FSI coupling model parameters should be entered. Since FCBI-C elements are used in fluid model, only iterative FSI analysis can be performed. Maximum number of fluid-structure iterations are set to 15 by ADINA as default. Also the tolerance values are the default values determined by ADINA. After numerous trials, the appropriate relaxation factors are determined. If an appropriate relaxation factor is not selected, then the solution can not converge. The Figure A.12 shows mentioned parameters related with FSI solution and relaxation factors.

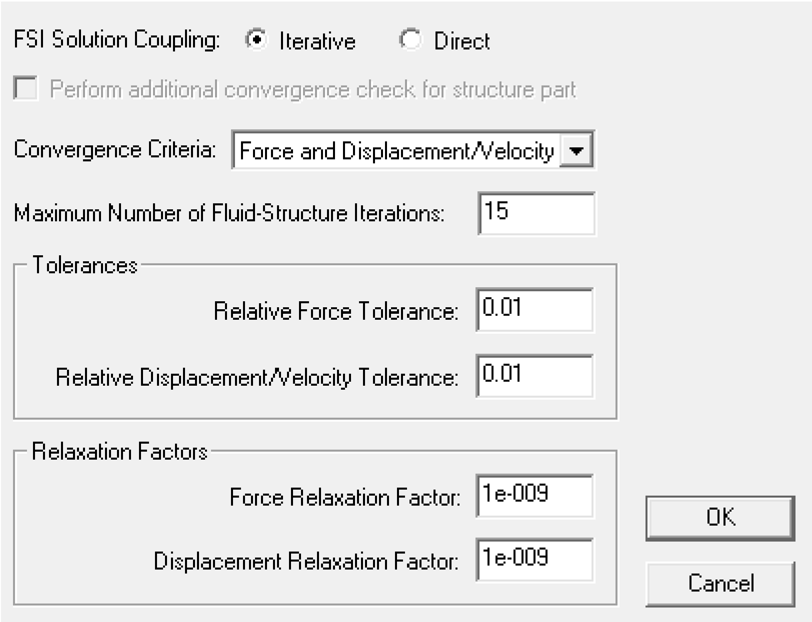

Figure A.12 FSI solution parameters

(ADINA CFD → FSI Options)

A similar modification needs to be performed in the structure model. The FSI mode should be activated and 'Dynamics-Implicit' option should be selected. Then the structure model will be coupled and time steps and time functions of flow model will be used for FSI coupled solution. The fluid-structure interface surfaces should be defined for both fluid and structure models. The fluid-structure boundary conditions will be defined in fluid model **(ADINA CFD → Model → Special Boundary Conditions)** and structure model **(ADINA Structures → Model → Boundary Conditions → FSI Boundary)** separately. After activating FSI modes in flow and structure models and defining fluid-structure interface surfaces then these two models can be coupled by using ADINA-FSI solver.

A.4. Post Processing in ADINA

The results can be viewed by using ‘Post Processing’ section of ADINA. The file created for post-processing by ADINA is called a ‘porthole’ file. The size of the file becomes higher as the mesh size and number of total time steps increase. In order to minimize the size of the ‘porthole’ files, the results are recorded only at the nodes of the wall. It should be noted that there should be a free memory space of approximately three times larger than the porthole file. If there is not enough memory, the results can not be viewed. By only recording the nodes at the wall, the porthole file minimized by 4 times.

APPENDIX B

MATLAB CODE TO PERFORM FFT FOR MONITORING ACOUSTIC PRESSURE

```
clear
clc
long=4096;
Fs = 4096;                    % Sampling frequency
T = 1/Fs;                     % Sample time
L = long;                     % Length of signal
t = (0:L-1)*T;                % Time vector
%%% Loading time history data from text files
XCoor = load('xcoordinates.txt');
XCoor=XCoor-0.05;
XCoor=XCoor*1000;
for i=1:155
   path = [int2str(i) '.txt'];
   X(i,:,:) =load(path);
   A(i,:) = X(i,:,2);
end
for i=1:155
   for j=1:long
   B(i,j)=A(i,j);
   end
end
```

```
A=B;
A=A+2000;

%%% Hanning Window %%%
w=window(@hann,long);
w=w/(sum(w)/length(w));
w=w';
for i=1:155
  A(i,:)=A(i,:).*w;
end
%%% FFT %%
for i=1:155
NFFT=long;
Y = fft(A(i,:),NFFT)/L;
M(i,:)=2*abs(Y(1:NFFT/2+1));
f = Fs/2*linspace(0,1,NFFT/2+1);
end
M_dB=20*log10(M);
surf(f,XCoor,M_dB,'LineStyle','none');
shading interp;
xlabel('Frequency (Hz)')
ylabel('Axial distance downstream of constriction exit
(mm)')
view([-270 -90]);
caxis([-100 0]);
colorbar;
xlim([0 600])
ylim([0 100])
```

APPENDIX C

MATLAB CODE TO PERFORM FFT FOR MONITORING NORMALIZED ACOUSTIC PRESSURE

```
clear
clc
long=4096;
Fs = 4096;                    % Sampling frequency
T = 1/Fs;                     % Sample time
L = long;                     % Length of signal
t = (0:L-1)*T;                % Time vector

%%% Loading time history data from text files
XCoor = load('xcoordinates.txt');
XCoor=XCoor-0.05;
XCoor=XCoor*1000;
for i=1:122
   path = [int2str(i) '.txt'];
   X(i,:,:) =load(path);
   A(i,:) = X(i,:,2);
end
for i=1:122
   for j=1:long
   B(i,j)=A(i,j);
   end
```

```
end
A=B;
A=A+2000;
%%% Hanning Window %%%
w=window(@hann,long);
w=w/(sum(w)/length(w));
w=w';
for i=1:122
  A(i,:)=A(i,:).*w;
end
%%% FFT %%
for i=1:122
NFFT=long;
Y = fft(A(i,:),NFFT)/L;
M(i,:)=2*abs(Y(1:NFFT/2+1));
f = Fs/2*linspace(0,1,NFFT/2+1);
end
maximum=max(M);
%% Scaled Pressures according to maximum pressure
maxim=max(maximum);
M_dB=20*log10(M/maxim);
surf(f,XCoor,M_dB,'LineStyle','none');

shading interp;
xlabel('Frequency (Hz)')
ylabel('Axial distance downstream of constriction exit
(mm)')
view([-270 -90]);
caxis([-200 0]);
colorbar;
xlim([0 600])
ylim([0 100])
```

APPENDIX D

MATLAB CODE TO MONITOR EMPIRICAL RESULTS OF TOBIN AND CHANG [22]

```
%%% MATLAB CODE USED TO FOR AMPIRICAL DATA OBTAINED BY
TOBIN AND CHANG

clear
clc
       p1 =     0.07057  ;          % The values found
for curve fit
       p2 =      0.3849  ;
       q1 =      -23.22  ;
       q2 =       167.9  ;

x1=1:1:100;
f1=1:1:600;
D=6.4;
% Unconstricted tube diameter in mm
d=2.3;
% Constricted tube diameter in mm
U=156;
% Velocity in mm/s

for x=1:1:100
% Pressure fluctuations are found
```

```
    for f=1:600
    p(x,f)=1.82*((p1*x + p2) / (x^2 + q1*x + q2))...
    *0.001*U^(1.5)*(D^2.5/d^2)*...
    (1+(20*((f*d^2)/(U*D))^5.3))^-0.5;
    end
end
p_dB=20*log10(p);
% Acoustic pressures are found

%   maximum=max(p);
% These 3 lines are used to find normalized acoustic
pressures
%   maxim=max(maximum);
%   p_dB=20*log10(p/maxim);

surf(f1,x1,p_dB,'LineStyle','none'); % Figure properties
shading interp;
xlabel('Frequency (Hz)')
ylabel('Axial distance downstream of constriction exit
(mm)')
view([-270 -90]);
caxis([-100 0]);
colorbar;
xlim([0 600])
ylim([0 100])
```

APPENDIX E

MATLAB CODE TO PERFORM FFT FOR MONITORING SPECTRAL RADIAL VELOCITY

```
clear
clc
long=4096;
Fs = 4096;                    % Sampling frequency
T = 1/Fs;                     % Sample time
L = long;                     % Length of signal
t = (0:L-1)*T;                % Time vector

%%% Loading time history data from text files
XCoor = load('xcoordinates.txt');
XCoor=XCoor-0.05;
XCoor=XCoor*1000;
for i=1:201
   path = [int2str(i) '.txt'];
   X(i,:,:) =load(path);
   A(i,:) = X(i,:,2);
end

for i=1:201
   for j=1:long
   B(i,j)=A(i,j);
```

```
   end
end
A=B;

%%% Hanning Window %%%
w=window(@hann,long);
w=w/(sum(w)/length(w));
w=w';
for i=1:201
  A(i,:)=A(i,:).*w;
end

%%% FFT %%
for i=1:201
NFFT=long;
Y = fft(A(i,:),NFFT)/L;
M(i,:)=2*abs(Y(1:NFFT/2+1));
f = Fs/2*linspace(0,1,NFFT/2+1);
end

M_dB=20*log10(M);
surf(f,XCoor,M_dB,'LineStyle','none');

shading interp;
xlabel('Frequency (Hz)')
ylabel('Axial distance downstream of constriction exit
(mm)')
view([-270 -90]);
caxis([-300 -200]);
colorbar;
xlim([0 600])
ylim([0 100])
```